# A Phase-Field Description for Pressurized and Non-Isothermal Propagating Fractures

**Nima Noii and Thomas Wick**

AG Wissenschaftliches Rechnen
Institut für Angewandte Mathematik
Leibniz Universität Hannover
Welfengarten 1, 30167 Hannover, Germany

# A Phase-Field Description for Pressurized and Non-Isothermal Propagating Fractures

Nima Noii[a], Thomas Wick[a,*]

[a]*Leibniz Universität Hannover, Institut für Angewandte Mathematik, AG Wissenschaftliches Rechnen, Welfengarten 1, 30167 Hannover, Germany*

## Abstract

In this work, we extend a phase-field approach for pressurized fractures to non-isothermal settings. Specifically, the pressure and the temperature are given quantities and the emphasis is on the correct modeling of the interface laws between a porous medium and the fracture. The resulting model is augmented with thermo-dynamical arguments and then analyzed from a mechanical perspective. The numerical solution is based on a robust semi-smooth Newton approach in which the linear equation systems are solved with a generalized minimal residual method and algebraic multigrid preconditioning. The proposed modeling and algorithmic developments are substantiated with different examples in two- and three dimensions. We notice that for some of these configurations manufactured solutions can be constructed, allowing for a careful verification of our implementation. Furthermore, crack-oriented predictor-corrector adaptivity and a parallel implementation are used to keep the computational cost reasonable. Snapshots of iteration numbers show an excellent performance of the nonlinear and linear solution algorithms. Lastly, for some tests, a computational analysis of the effects of strain-energy splitting is performed, which has not been undertaken to date for similar phase-field settings involving pressure, fluids or non-isothermal effects.

## 1. Introduction

In subsurface hydraulic fractures, it is known that cold injections (e.g., fluids or $CO2$) may open and advance fractures [23, 46, 21, 13, 45, 16, 41, 40, 38]. These effects play a role in oil/gas production, $CO2$ storage, and geothermal energy production. For instance, [21] investigated the effects of cold-water injection on the growth and decay of a pre-existing crack when pressure and temperature are taken into account. They developed an analytical formula to solve their model. Another study incorporating thermal effects was conducted in [13]. Therein, the fracture propagation is based on the displacement discontinuity method. For similar computations the displacement discontinuity method was used in [22]. In [46], the interaction of temperature and fluid stresses with respect to wellbores have been investigated. The authors show that warm fluids avoid (or restrict) fracture development. Recently, [41, 40] studied $CO2$ injections and their influence on the fracture aperture/growth and a thermo-hydro-mechanical approach for fractured geothermal systems.

In the previously mentioned studies, different numerical discretization techniques were adopted. A popular variational approach to fracture was introduced in [18] (with according numerics presented in [8]) and which was complemented with thermodynamical arguments in [4] and [33, 31]. In the last study, the alternative name phase-field fracture was given. The extension of phase-field to hydraulic fractures in poroelasticity

---

was first undertaken in [35] (originally published as ICES preprint [34]). Therein the solution of the fluid equation (of Darcy type) was assumed to be given, yielding a given pressure for the poroelastic mechanics step. On the other hand, phase-field models involving thermal effects in pure elasticity or plasticity have been studied in [11, 32, 30].

The setting presented in [35] constitutes the starting point to formulate the mechanics step of a *phase-field fracture model in thermo-poroelasticity* with pressure and temperature as given quantities. For the temperature contribution, an elliptic diffusion equation is considered from which a time-dependent decline constant can be derived; see Hagoort [23]. This parameter controls the thermo-poroelastic stress (also called back-stress). Based on analytical formulas derived by Sneddon and Lowengrub [43, 44] for the crack opening displacements (COD, aperture) for pressurized fractures in an elastic medium, Hagoort extended these equations to non-isothermal situations [23]. A very detailed derivation and discussions of the application in thermo-poroelasticity can be found in Tran et al. [45].

In this paper, we follow the ideas outlined in [45] and develop a phase-field model for pressurized and non-isothermal fractures. Here, we use the ideas from [35] and carefully derive interface conditions between the thermo-poroelastic medium and the fracture. The resulting models (i.e., the energy functional and the related Euler-Lagrange equations) are then analyzed in detail from a mechanical perspective. Here, the focus is on thermodynamical arguments and strain-energy splitting, which are also complemented with corresponding numerical tests.

Our proposed model is implemented into the adaptive parallel framework developed in [24, 50, 29] with most recent results on its computational performance provided in [25]. A key purpose in the current work is on a detailed code verification with respect to the chosen discretization, robustness and efficiency. Therefore, some of our settings (in 2D and 3D) are compared with manufactured solutions developed in [45]. Moreover, in some tests, a computational analysis of the effects of strain-energy splitting is performed in order to study the influence in pressurized and non-isothermal fracture propagation. Iteration numbers of the linear solver and the evolution of the nonlinear residual and the primal-dual active set (enforcing the crack irreversibility constraint) method are undertaken to study the performance of the numerical algorithms.

The outline of this paper is as follows: In Section 2 a phase-field model accounting for given pressures and given temperatures is derived. Then, in Section 3 the model is augmented with thermodynamical arguments and then analyzed from a mechanical perspective. The final model and the numerical solution are discussed in Section 4. Several tests demonstrating our developed model are presented in Section 5. Here, comparisons to analytical solutions, grid refinement studies, calculation of quantities of interest such as the aperture, adaptive studies and the performance of the nonlinear and linear solvers are provided. In Section 6 our main findings are summarized.

## 2. Non-isothermal and pressurized phase-field modeling

In the following, let $\Omega \in \mathbb{R}^d$, $d = 2, 3$ be a smooth open and bounded set. In $\Omega$, a lower dimensional fracture is denoted by $C \in \mathbb{R}^{d-1}$. We assume either Dirichlet boundaries conditions $\partial\Omega_D := \partial\Omega$ and Neumann condition on $\partial_N\Omega := \Gamma_N \cup \partial C$, where $\Gamma_N$ denotes the outer domain boundary and $\partial C$ the crack boundary. Let $I := (0, T)$ denote the loading/time interval with $T > 0$ being the end time value.

Prototype configurations of the setting are illustrated in Fig. 1. Using a phase-field approach, the surface fracture $C$ is approximated in $\Omega_F \subset \Omega \in \mathbb{R}^d$. The intact region, where with no fracture denoted as $\Omega_R := \Omega\backslash\Omega_F \subset \Omega \in \mathbb{R}^d$ such that $\Omega_R \cup \Omega_F = \Omega$ and $\Omega_R \cap \Omega_F = \varnothing$. It has to be noted, that $\Omega_F$, i.e. the domain in which the smeared crack phase-field is approximated, and its boundary $\partial\Omega_F$ strongly depend on the choice of the phase-field regularization parameter, i.e. $\varepsilon > 0$.

We deal with a multi-field problem depending on the displacement field $\boldsymbol{u} : \Omega \to \mathbb{R}^d$ and the crack phase-field $\varphi : \Omega \to [0, 1]$ for a given pressure $p : \Omega \to \mathbb{R}$ and a given temperature $\Theta : \Omega \to \mathbb{R}$. The limiting values of $\varphi$, namely, $\varphi = 1$ and $\varphi = 0$ represent the undamaged and fully broken material phases, respectively. Finally, we, denote the $(\cdot, \cdot)$ the standard $L^2$ scalar product in the domain $\Omega$ and $\langle\cdot, \cdot\rangle$ the $L^2$ scalar product on a boundary part.
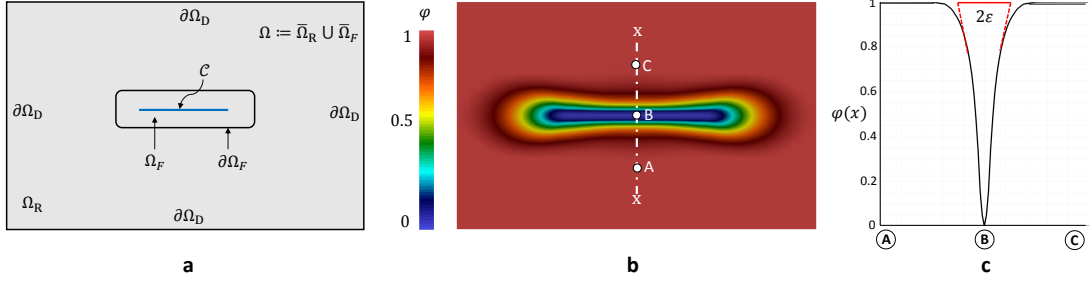
Figure 1: (a) Setup of the notation: the unbroken domain is denoted by $\Omega$ and $C$ is the crack phase-field. The smeared crack phase-field is approximated by the domain $\Omega_F$. The half thickness of $\Omega_F$ is $\varepsilon$. The fracture boundary is $\partial\Omega_F$ and the outer boundary of the domain is $\partial\Omega$.(b) The corresponding realization using phase-field is shown. Here, the lower-dimensional fracture ($\varphi = 0$) is approximated with the phase-field variable. Consequently, $\Omega_F$ can be represented in terms of $\varphi$. (c) The transition zone with $0 < \varphi < 1$ has the thickness of $2\varepsilon$ where the crack profile on the section $x - x$ shown in (b) is obtained through a finite element method for solving the multi-field (i.e. $u$ and $\varphi$) problem.

### 2.1. The energy functional in the thermo-poroelastic medium

We start with the following energy functional posed in the thermo-poroelastic medium:

$$\mathcal{E}(u) = \frac{1}{2}(\sigma, \varepsilon(u))_\Omega - \langle\tau, u\rangle_{\partial_N\Omega}, \tag{1}$$

where $\sigma$ is the stress tensor specified below, $\varepsilon(u)$ is the linearized strain tensor and $\tau$ traction forces on the boundaries $\partial_N\Omega := \Gamma_N \cup \partial C$. For the specific definition of the thermo-poroelastic stress, we apply the constitutive expression derived in [15]:

$$\sigma = \sigma_0 + \sigma_\varepsilon - \alpha_B(p - p_0)I - 3\alpha_\Theta K_d(\Theta - \Theta_0)I.$$

Here, $\sigma_0$ is the initial stress, $\alpha_B$ is Biot's constant, $p$ is the pressure, $p_0$ is the initial pressure, $I$ is the second order identity tensor, $3\alpha_\Theta$ is the volumetric skeleton thermal dilation coefficient (or thermal expansion coefficient). Then, $K_d := \frac{2}{d}\mu + \lambda$ ($d \in \{2, 3\}$ still refers to the dimension of problem), $\Theta$ is the temperature, and $\Theta_0$ is the initial temperature, and

$$\sigma_\varepsilon = 2\mu\varepsilon + \lambda tr(\varepsilon)I, \quad \varepsilon(u) = \frac{1}{2}(\nabla u + \nabla u^T),$$

where $\mu$ and $\lambda$ are positive material parameters.

Using these definitions and setting $\sigma_0 = 0$ (for the convenience of the reader), we can write the energy functional in the thermo-poroelastic domain:

$$\begin{aligned}
\mathcal{E}(u) &= \frac{1}{2}(\sigma, \varepsilon(u))_\Omega - \langle\tau, u\rangle_{\partial_N\Omega} \\
&= \frac{1}{2}(\sigma_\varepsilon, \varepsilon(u))_\Omega - \langle\tau, u\rangle_{\partial_N\Omega} - (\alpha_B(p - p_0), \nabla \cdot u) - (3\alpha_\Theta K_d(\Theta - \Theta_0), \nabla \cdot u).
\end{aligned} \tag{2}$$

This functional represents the energy in the thermo-poroelastic domain only. For the total energy, we need to account for the crack energy as well. In the presence of a fracture $C$, we need to add the fracture energy which is expressed through [18]:

$$G_c\mathcal{H}^{d-1}(C),$$

where $G_c$ is the critical elastic energy restitution rate (related to the stress intensity factor through Irvins formula) and $\mathcal{H}^{d-1}$ is the $d - 1$-dimensional Hausdorff measure.

3

Then, we arrive at the total energy functional:

$$\mathcal{E}(\boldsymbol{u}, C) = \frac{1}{2}(\boldsymbol{\sigma}_\varepsilon, \boldsymbol{\varepsilon}(\boldsymbol{u}))_\Omega - \langle \boldsymbol{\tau}, \boldsymbol{u} \rangle_{\partial_N \Omega} - (\alpha_B(p - p_0), \nabla \cdot \boldsymbol{u}) - (3\alpha_\Theta K_d(\Theta - \Theta_0), \nabla \cdot \boldsymbol{u})$$
$$+ G_c \mathcal{H}^{d-1}(C). \tag{3}$$

This functional is composed by contributions of two disjunct domains, namely $\Omega$ and $C$. For the numerical treatment we regularize (3) following [8]. Specifically, the crack energy is approximated through a sequence of elliptic problems, so-called Ambrosio-Tortorelli functionals [2, 3]. Therein, $\mathcal{H}^{d-1}$ is regularized by introducing an additional smoothed indicator variable nowadays called phase-field: $\varphi : \Omega \to [0, 1]$. Finally, we account for the crack irreversibility constraint that the crack can only grow:

$$\partial_t \varphi \le 0. \tag{4}$$

For stating the variational formulations, we now introduce three sets:

$$V := H_0^1(\Omega)^d, \quad W := H^1(\Omega), \quad W_{in} := \{\varphi \in H^1(\Omega)| \ 0 \le \varphi \le \varphi^{old}\}.$$

As typical in problems with inequality constraints (see e.g., [27, 28]), $W_{in}$ is a nonempty, closed, convex, subset of the linear function space $W$. Due to the inequality constraint (4), $W_{in}$ is not anymore a linear space.

Moreover, we recall that we do not deal with a classical time-dependent problem, but a quasi-static load-incremental evolution, for which the loading interval is discretized using the discrete time (loading) points

$$0 = t_0 < t_1 < \ldots < t_n < \ldots < t_N = T.$$

With these preparations, the energy functional (3) can be written as:

**Formulation 2.1** (Regularized energy functional). *Let $p_0, p, \Theta, \Theta_0$ to be given with the initial conditions $\boldsymbol{u}_0 = \boldsymbol{u}(x, 0)$ and $\varphi_0 = \varphi(x, 0)$. For the loading increments $n = 1, 2, \ldots, N$, find $\boldsymbol{u} := \boldsymbol{u}^n \in V$ and $\varphi := \varphi^n \in W_{in}$ such that:*

$$\mathcal{E}_\varepsilon(\boldsymbol{u}, \varphi) = \underbrace{\frac{1}{2}(((1 - \kappa)\varphi^2 + \kappa)\boldsymbol{\sigma}_\varepsilon, \boldsymbol{\varepsilon}(\boldsymbol{u}))_\Omega}_{\text{mechanical term}} - \underbrace{\langle \boldsymbol{\tau}, \boldsymbol{u} \rangle_{\Gamma_n \cup \partial C}}_{\text{external term}}$$
$$- \underbrace{(\alpha_B(p - p_0)\varphi^2, \nabla \cdot \boldsymbol{u})}_{\text{pressure term}} - \underbrace{(3\alpha_\Theta K_d(\Theta - \Theta_0)\varphi^2, \nabla \cdot \boldsymbol{u})}_{\text{thermal term}}$$
$$+ \underbrace{G_c \left( \frac{1}{2\varepsilon} \|1 - \varphi\|^2 + \frac{\varepsilon}{2} \|\nabla \varphi\|^2 \right)}_{\text{fracture term}}. \tag{5}$$

**Remark 2.1.** *Approximation of (5) without pressures $p, p_0$ and temperatures $\Theta, \Theta_0$ has been used in many studies for solid mechanics.*

**Remark 2.2.** *In (5), $\kappa := \kappa(h)$ is a positive regularization parameter for the elastic energy and $\varepsilon := \varepsilon(h)$ is a regularization parameter for the phase-field variable denoting the width of the transition zone in which $\varphi$ changes from 0 to 1; see Fig. 1.*

The stationary points of the energy functional (5) are characterized by the first-order necessary conditions, namely the so-called Euler-Lagrange equations, which are obtained by (formal) differentiation in the variables $\boldsymbol{u}$ and $\varphi$:

**Formulation 2.2** (Euler-Lagrange equations). *Let $p_0, p, \Theta, \Theta_0$ be given with the initial conditions $\boldsymbol{u}_0 = \boldsymbol{u}(x, 0)$ and $\varphi_0 = \varphi(x, 0)$. For the loading increments $n = 1, 2, \ldots, N$, find $\boldsymbol{u} := \boldsymbol{u}^n \in V$ and $\varphi := \varphi^n \in W_{in}$ such that:*

$$(((1 - \kappa)\varphi^2 + \kappa)\boldsymbol{\sigma}_\varepsilon, \boldsymbol{\varepsilon}(\boldsymbol{w})) - \langle \boldsymbol{\tau}, \boldsymbol{w} \rangle$$
$$- (\alpha_B(p - p_0)\varphi^2, \nabla \cdot \boldsymbol{w}) - (3\alpha_\Theta K_d(\Theta - \Theta_0)\varphi^2, \nabla \cdot \boldsymbol{w}) = 0 \quad \forall \boldsymbol{w} \in V,$$

*and*

$$(1 - \kappa)(\varphi \sigma_\varepsilon(\boldsymbol{u}) : \varepsilon(\boldsymbol{u}), \psi - \varphi)$$
$$- 2(\alpha_B - 1)((p - p_0)\nabla \cdot \boldsymbol{u}\,\varphi, \psi - \varphi) - 2(3\alpha_\Theta K_d)((\Theta - \Theta_0)\nabla \cdot \boldsymbol{u}\,\varphi, \psi - \varphi)$$
$$+ G_c(\frac{1}{\varepsilon}(\varphi - 1, \psi - \varphi) + \varepsilon(\nabla\varphi, \nabla(\psi - \varphi))) \geq 0 \quad \forall \psi \in W \cap L^\infty.$$

## 2.2. Incorporating fracture pressure and temperature

The energy functional (5) and the corresponding Euler-Lagrange equations in Formulation 2.2 are still incomplete because only mechanisms in the thermo-poroelastic medium are taken into account so far. In the following, we consider pressure and temperature variations in the fracture as well, acting as additional normal stresses on the interface between the thermo-poroelastic medium and the fracture. Hence, we obtain a modification of the normal stress term $\langle \boldsymbol{\tau}, \boldsymbol{u} \rangle_{\partial_N \Omega}$.

Similar to [35] in which an interface law was derived to account for pressurized fractures, we now derive an expression including temperature effects. For the convenience of understanding, we also recapitulate the steps of the pressure and develop the modified terms for the temperature simultaneously. Assuming that the fracture is a zone of high permeability and its width much smaller than its length, the leading order of the pressure stress in $C$ is

$$-(p - p_0)\boldsymbol{I}.$$

Similarly, we assume (according to [45]) that the leading order of the temperature stress in $C$ is given by

$$-C_\Theta(\Theta - \Theta_0)\boldsymbol{I}, \quad \text{with} \quad C_\Theta := C_\Theta(x, t).$$

The constant $C_\Theta$ is obtained by following [45] to get a relation for the temperature near the fracture. We briefly sketch the basic idea. Working with the heat conduction equation, while neglecting convection-dominated terms, we obtain:

$$\partial_t \Theta - \nabla \cdot (\kappa_\Theta \nabla \Theta) = 0, \tag{6}$$

with the thermal diffusivity $\kappa_\Theta = \frac{K_r}{\rho_r C_r}$, where $\rho_r$ is the rock density, $C_r$ is the specific heat, $K_r$ thermal conductivity. With the help of the heat conduction equation, a parameter measuring the gradient of the temperature at the fracture interface is derived. This law provides an heuristic argument for the temperature evolution without solving the full temperature equation in the whole domain. Specifically,

$$C_\Theta = A_\Theta \left( \frac{\lambda_\Theta}{2\lambda_\Theta + 1} \right), \quad A_\Theta = \frac{E_Y \beta}{1 - \nu_s}, \tag{7}$$

where $\beta$ is a linear thermal expansion coefficient, $E_Y$ is a Young's modulus, $\nu_s$ is a Poisson's ratio. The parameter $\lambda_\Theta$ is derived by Hagoort [23] based on the heat conduction equation. Then,

$$\lambda_\Theta = \sinh^{-1}(\frac{\gamma_T}{0.5 l_0} \sqrt{\pi \kappa_\Theta t}), \tag{8}$$

where $1 \leq \gamma_T \leq \frac{4}{\pi}$.

## 2.3. Interface laws for pressure and temperature

We pursue in the following by deriving an interface relationship between the thermo-poroelastic medium $\Omega$ and the fracture $C$. As usually required for coupled problems with interfaces, we need a kinematic and a dynamic coupling condition. The kinematic conditions are to enforce

$$p_f = p_R \quad \text{and} \quad \Theta_f = \Theta_R \quad \text{on } C,$$

5

where $p_f$ is the fracture pressure, $p_R$ the thermo-poroelastic pressure, $\Theta_f$ the temperature in the fracture and $\Theta_R$ the thermo-poroelastic temperature. Since we enforce continuity of these variables on $C$ we do not distinguish anymore in the rest of the paper and simply use $p$ and $\Theta$.

The dynamic coupling condition represents the continuity of normal stresses on the crack boundary $\partial C$ and can be written as

$$
\boldsymbol{\sigma n} = \underbrace{[\boldsymbol{\sigma}_0 + \boldsymbol{\sigma}_\varepsilon - \alpha_B(p - p_0)\boldsymbol{I} - 3\alpha_\Theta K_d(\Theta - \Theta_0)\boldsymbol{I}]}_{\text{Thermo-poroelastic stress}}\boldsymbol{n}
$$

$$
= -\underbrace{[(p - p_0) - C_\Theta(\Theta - \Theta_0)]}_{\text{Fracture stress}}\boldsymbol{n}. \tag{9}
$$

Since the fracture boundary is smeared and not explicitly known, it remains to discuss how the interface condition is imposed. The kinematic conditions are Dirichlet-like conditions and build into the function spaces as usually done. The dynamic conditions are re-written as domain integrals by using Gauss' divergence theorem. We recall that the entire boundary is composed as

$$
\langle \boldsymbol{\sigma n}, \boldsymbol{u} \rangle_{\partial_N \Omega} = \langle \boldsymbol{\tau}, \boldsymbol{u} \rangle_{\Gamma_N} + \langle \boldsymbol{\sigma n}, \boldsymbol{u} \rangle_{\partial C}.
$$

We now manipulate the last term with the help of Eq. 9 and the divergence theorem, reads

$$
\begin{aligned}
\langle \boldsymbol{\sigma n}, \boldsymbol{u} \rangle_{\partial C} &= -\langle (p - p_0)\boldsymbol{n}, \boldsymbol{u} \rangle_{\partial C} - \langle C_\Theta(\Theta - \Theta_0)\boldsymbol{n}, \boldsymbol{u} \rangle_{\partial C} \\
&= -(\nabla \cdot (p - p_0)\boldsymbol{u}) + \langle (p - p_0)\boldsymbol{n}, \boldsymbol{u} \rangle_{\Gamma_N} - (C_\Theta \nabla \cdot (\Theta - \Theta_0)\boldsymbol{u}) \\
&\quad + \langle C_\Theta(\Theta - \Theta_0)\boldsymbol{n}, \boldsymbol{u} \rangle_{\Gamma_N} \\
&= -((p - p_0), \nabla \cdot \boldsymbol{u}) - (\nabla(p - p_0), \boldsymbol{u}) + \langle (p - p_0)\boldsymbol{n}, \boldsymbol{u} \rangle_{\Gamma_N} \\
&\quad - (C_\Theta(\Theta - \Theta_0), \nabla \cdot \boldsymbol{u}) - (C_\Theta \nabla(\Theta - \Theta_0), \boldsymbol{u}) + \langle C_\Theta(\Theta - \Theta_0)\boldsymbol{n}, \boldsymbol{u} \rangle_{\Gamma_N}.
\end{aligned} \tag{10}
$$

These terms can be combined with the other terms containing pressures and temperatures in the energy functional (5):

$$
(\alpha_B(p - p_0), \nabla \cdot \boldsymbol{u}) \quad \text{and} \quad (3\alpha_\Theta K_d(\Theta - \Theta_0), \nabla \cdot \boldsymbol{u}).
$$

In total we obtain (noticing that all signs change because we deal with $-\langle \boldsymbol{\sigma n}, \boldsymbol{u} \rangle_{\partial_N \Omega}$ in (5)):

$$
\begin{aligned}
&- \langle \boldsymbol{\sigma n}, \boldsymbol{u} \rangle_{\partial_N \Omega} - (\alpha_B(p - p_0), \nabla \cdot \boldsymbol{u}) - (3\alpha_\Theta K_d(\Theta - \Theta_0), \nabla \cdot \boldsymbol{u}) \\
&= -\langle \boldsymbol{\tau}, \boldsymbol{u} \rangle_{\Gamma_N} - \langle \boldsymbol{\sigma n}, \boldsymbol{u} \rangle_C - (\alpha_B(p - p_0), \nabla \cdot \boldsymbol{u}) - (3\alpha_\Theta K_d(\Theta - \Theta_0), \nabla \cdot \boldsymbol{u}) \\
&= -\langle \boldsymbol{\tau}, \boldsymbol{u} \rangle_{\Gamma_N} - (\alpha_B(p - p_0), \nabla \cdot \boldsymbol{u}) + ((p - p_0), \nabla \cdot \boldsymbol{u}) + (\nabla(p - p_0), \boldsymbol{u}) \\
&\quad + \langle (p - p_0)\boldsymbol{n}, \boldsymbol{u} \rangle_{\Gamma_N} - (3\alpha_\Theta K_d(\Theta - \Theta_0), \nabla \cdot \boldsymbol{u}) + (C_\Theta(\Theta - \Theta_0), \nabla \cdot \boldsymbol{u}) \\
&\quad + (C_\Theta \nabla(\Theta - \Theta_0), \boldsymbol{u}) + \langle C_\Theta(\Theta - \Theta_0)\boldsymbol{n}, \boldsymbol{u} \rangle_{\Gamma_N}.
\end{aligned} \tag{11}
$$

To complete, we introduce a phase-field representation of Eq. 11 and weight the domain terms with $\varphi^2$ (see Section 2 in [35] for pressurized fractures only) in (5), which then yields:

**Formulation 2.3** (Energy functional including fracture pressure and temperature). *Let $p_0, p, \Theta, \Theta_0$ be given with an initial condition $\boldsymbol{u}_0 = \boldsymbol{u}(x, 0)$ and $\varphi_0 = \varphi(x, 0)$. For the loading increments $n = 1, 2, \ldots, N$, find*

$\boldsymbol{u} := \boldsymbol{u}^n \in V$ and $\varphi := \varphi^n \in W_{in}$ such that:

$$\mathcal{E}_\varepsilon(\boldsymbol{u}, \varphi) = \underbrace{\frac{1}{2}(((1 - \kappa)\varphi^2 + \kappa)\boldsymbol{\sigma}_\varepsilon(\boldsymbol{u}), \boldsymbol{\varepsilon}(\boldsymbol{u}))_\Omega}_{\text{Mechanical term}} - \underbrace{\langle \tilde{\boldsymbol{\tau}}, \boldsymbol{u} \rangle_{\Gamma_N}}_{\text{External load}}$$

$$- \underbrace{((\alpha_B - 1)(p - p_0)\varphi^2, \nabla \cdot \boldsymbol{u}) + (\nabla(p - p_0)\varphi^2, \boldsymbol{u})}_{\text{Pressure term}}$$

$$- \underbrace{((3\alpha_\Theta K_d + C_\Theta)(\Theta - \Theta_0)\varphi^2, \nabla \cdot \boldsymbol{u}) + (C_\Theta \nabla(\Theta - \Theta_0)\varphi^2, \boldsymbol{u})}_{\text{Thermal term}}$$

$$+ \underbrace{G_c\left(\frac{1}{2\varepsilon}\|1 - \varphi\|^2 + \frac{\varepsilon}{2}\|\nabla\varphi\|^2\right)}_{\text{Fracture term}},$$

where $\tilde{\boldsymbol{\tau}} = \boldsymbol{\tau} - (p - p_0)\boldsymbol{n} + C_\Theta(\Theta - \Theta_0)\boldsymbol{n}$.

**Remark 2.3.** *We underline again that $p$ and $\Theta$ are fixed and given in this paper and therefore not solution variables. The extension in which $p$ is also an unknown was first proposed in [36]. A similar development for non-isothermal phase-field fractures in thermo-poroelasticity is ongoing work.*

**Remark 2.4.** *We notice that the temperature opens the crack if $\Theta < \Theta_0$ (see also Remark 3.3), i.e., the current (or injected) temperature is lower than the initial temperature.*

**Remark 2.5.** *When normal stresses (traction forces) are prescribed on (parts of) the boundary, the term $\tilde{\boldsymbol{\tau}} = \boldsymbol{\tau} - (p - p_0)\boldsymbol{n} + C_\Theta(\Theta - \Theta_0)\boldsymbol{n}$ must be carefully considered; see [42] or [35][Section 5.2].*

## 3. Thermodynamic arguments and mechanical analysis

In this section, we further augment our proposed model with thermodynamic arguments and subsequently analyze our model from a mechanical point of view.

### 3.1. Extension to a decoupled strain-energy function into volumetric and isochoric response

Since the fracturing material behaves quite differently in bulk and shear parts of the domain, we employ a consistent split for the strain energy density function, i.e.

$$\Psi(\boldsymbol{\varepsilon}(\boldsymbol{u})) := \frac{\lambda}{2}\big(\boldsymbol{\varepsilon}(\boldsymbol{u}) : \boldsymbol{I}\big)^2 + \mu\boldsymbol{\varepsilon}(\boldsymbol{u})^2 : \boldsymbol{I}.$$

Hence, instead of dealing directly with $\boldsymbol{\varepsilon}(\boldsymbol{u})$, we perform additive decomposition of strain tensor into *volume-changing* (volumetric part) and *volume-preserving* (deviatoric part), i.e.

$$\boldsymbol{\varepsilon}(\boldsymbol{u}) = \boldsymbol{\varepsilon}^{vol}(\boldsymbol{u}) + \boldsymbol{\varepsilon}^{dev}(\boldsymbol{u}).$$

Here, the volumetric strain is denoted as $\boldsymbol{\varepsilon}^{vol}(\boldsymbol{u}) := \frac{1}{3}(\boldsymbol{\varepsilon}(\boldsymbol{u}) : \boldsymbol{I})\boldsymbol{I}$ and the deviatoric strain is denoted as $\boldsymbol{\varepsilon}^{dev}(\boldsymbol{u}) := \mathbb{P} : \boldsymbol{\varepsilon}$. The fourth-order projection tensor $\mathbb{P} := \mathbb{I} - \frac{1}{3}\boldsymbol{I} \otimes \boldsymbol{I}$ is introduced to map the full strain tensor to its deviatoric counterpart. Therein, $\mathbb{I}_{i,j,k,l} := \frac{1}{2}\big(\delta_{i,k}\delta_{j,l} + \delta_{i,l}\delta_{j,k}\big)$ is the fourth-order symmetric identity tensor. Furthermore, $\mathbb{P}$ possesses the major symmetries, i.e. $\mathbb{P}_{i,j,k,l} = \mathbb{P}_{k,l,i,j}$, and $\mathbb{P}^n = \mathbb{P}$ for any given integer $n$. So, a decoupled representation of the strain-energy function into a so-called volumetric and deviatoric contribution are given as follows,

$$\Psi(\boldsymbol{\varepsilon}(\boldsymbol{u})) = \Psi(\boldsymbol{\varepsilon}^{vol}(\boldsymbol{u})) + \Psi(\boldsymbol{\varepsilon}^{dev}(\boldsymbol{u})). \tag{12}$$

Therein, the volumetric contribution of the strain energy density function reads,

7

$$\Psi(\boldsymbol{\varepsilon}^{vol}(\boldsymbol{u})) := \frac{\lambda}{2}\Big(\boldsymbol{\varepsilon}^{vol}(\boldsymbol{u}) : \boldsymbol{I}\Big)^2 + \mu\boldsymbol{\varepsilon}^{vol}(\boldsymbol{u})^2 : \boldsymbol{I} = \frac{K_d}{2}(\boldsymbol{\varepsilon}^{vol}(\boldsymbol{u}) : \boldsymbol{I})^2, \tag{13}$$

where $K_d := \frac{2}{d}\mu + \lambda$ is the bulk modulus and $d \in \{2, 3\}$. The deviatoric contribution of the strain energy density function is

$$\Psi(\boldsymbol{\varepsilon}^{dev}(\boldsymbol{u})) := \frac{\lambda}{2}\Big(\boldsymbol{\varepsilon}^{dev}(\boldsymbol{u}) : \boldsymbol{I}\Big)^2 + \mu\boldsymbol{\varepsilon}^{dev}(\boldsymbol{u})^2 : \boldsymbol{I} = \mu\boldsymbol{\varepsilon}^{dev}(\boldsymbol{u})^2 : \boldsymbol{I}. \tag{14}$$

To show that equality holds in Eq.12, the identities $\boldsymbol{\varepsilon}^{dev}(\boldsymbol{u}) : \boldsymbol{I} = 0$ and $\boldsymbol{\varepsilon}^{vol}(\boldsymbol{u}) : \boldsymbol{\varepsilon}^{dev}(\boldsymbol{u}) = 0$ are used. Physically, it is trivial to assume that the degradation induced by the phase field acts only on the tensile and shear counterpart of the elastic strain density function. Hence, it is assumed there is no degradation in compression, which also prevents interpenetration of the crack lips during crack closure [1]. It turns out that the modified strain energy density function for the fracturing material becomes,

$$\Psi\big(\boldsymbol{\varepsilon}(\boldsymbol{u})\big) := g(\varphi)\Psi^+\big(\boldsymbol{\varepsilon}(\boldsymbol{u})\big) + \Psi^-\big(\boldsymbol{\varepsilon}(\boldsymbol{u})\big), \tag{15}$$

such that a monotonically decreasing quadrature degradation function, i.e.

$$g(\varphi) := (1 - \kappa)\varphi^2 + \kappa, \tag{16}$$

describes the degradation of the solid with the evolving crack phase-field parameter $\varphi$, includes $\kappa$ that is a small residual stiffness that is introduced to prevent numerical problems. Additionally, the positive part of the strain energy density function that is the tensile and deviatoric part of full strain energy density function reads

$$\Psi^+(\boldsymbol{\varepsilon}(\boldsymbol{u})) = H^+(\nabla.\boldsymbol{u})\Psi(\boldsymbol{\varepsilon}^{vol}(\boldsymbol{u})) + \Psi(\boldsymbol{\varepsilon}^{dev}(\boldsymbol{u})). \tag{17}$$

Therein, $H^+(\nabla.\boldsymbol{u})$ is a *positive Heaviside function* such that if $\nabla.\boldsymbol{u}$ is positive return one and otherwise, give zero value. It is noted due to identity $\nabla.\boldsymbol{u} = \mathrm{tr}(\boldsymbol{\varepsilon})$, the positive Heaviside function indicates the points in a domain where they are in tensile part, i.e. $H^+(\nabla.\boldsymbol{u}) = 1$ and compression part, i.e. $H^+(\nabla.\boldsymbol{u}) = 0$. Negative strain energy density function that is the compression part of the full strain energy density function, is

$$\Psi^-(\boldsymbol{\varepsilon}(\boldsymbol{u})) = \Big(1 - H^+(\nabla.\boldsymbol{u})\Big)\Psi(\boldsymbol{\varepsilon}^{vol}(\boldsymbol{u})). \tag{18}$$

The constitutive equation for the modified strain energy density function, whereas the stress response constitutes an additive split of $\boldsymbol{\sigma}_{\boldsymbol{\varepsilon}} := \frac{\partial\Psi(\boldsymbol{\varepsilon})}{\partial\boldsymbol{\varepsilon}}$ to purely tensile contribution, i.e. $\boldsymbol{\sigma}_{\boldsymbol{\varepsilon}}^+(\boldsymbol{\varepsilon})$ and a purely compression contribution, i.e. $\boldsymbol{\sigma}_{\boldsymbol{\varepsilon}}^-(\boldsymbol{\varepsilon})$, reads

$$\boldsymbol{\sigma}_{\boldsymbol{\varepsilon}} := \frac{\partial\Psi(\boldsymbol{\varepsilon}}{\partial\boldsymbol{\varepsilon}} = g(\varphi)\frac{\partial\Psi^+(\boldsymbol{\varepsilon})}{\partial\boldsymbol{\varepsilon}} + \frac{\partial\Psi^-(\boldsymbol{\varepsilon})}{\partial\boldsymbol{\varepsilon}} = g(\varphi)\boldsymbol{\sigma}_{\boldsymbol{\varepsilon}}^+(\boldsymbol{\varepsilon}) + \boldsymbol{\sigma}_{\boldsymbol{\varepsilon}}^-(\boldsymbol{\varepsilon}). \tag{19}$$

Therein,

$$\boldsymbol{\sigma}_{\boldsymbol{\varepsilon}}^+(\boldsymbol{\varepsilon}) = K_n H^+(\nabla.\boldsymbol{u})(\boldsymbol{\varepsilon} : \boldsymbol{I})\boldsymbol{I} + 2\mu\boldsymbol{\varepsilon}^{dev}, \quad \text{and} \quad \boldsymbol{\sigma}_{\boldsymbol{\varepsilon}}^-(\boldsymbol{\varepsilon}) = K_n\Big(1 - H^+(\nabla.\boldsymbol{u})\Big)(\boldsymbol{\varepsilon} : \boldsymbol{I})\boldsymbol{I}.$$

The decoupled representation of the fourth-order elasticity tensor to relate the work into conjugate pairs of stress and strain tensor by means of additive decomposition of the stress tensor, reads

$$\mathbb{C} := \frac{\partial\boldsymbol{\sigma}(\boldsymbol{\varepsilon})}{\partial\boldsymbol{\varepsilon}} = g(\varphi)\frac{\partial\boldsymbol{\sigma}^+(\boldsymbol{\varepsilon})}{\partial\boldsymbol{\varepsilon}} + \frac{\partial\boldsymbol{\sigma}^-(\boldsymbol{\varepsilon})}{\partial\boldsymbol{\varepsilon}} =: g(\varphi)\mathbb{C}^+ + \mathbb{C}^-, \tag{20}$$

with

$$\mathbb{C}^+ = K_n H^+(\nabla.\boldsymbol{u})\boldsymbol{I} \otimes \boldsymbol{I} + 2\mu\mathbb{P}, \quad \text{and} \quad \mathbb{C}^- = K_n\Big(1 - H^+(\nabla.\boldsymbol{u})\Big)\boldsymbol{I} \otimes \boldsymbol{I},$$

where the identity $\frac{\partial\boldsymbol{\varepsilon}^{dev}(\boldsymbol{u})}{\partial\boldsymbol{\varepsilon}(\boldsymbol{u})} = \mathbb{P}$ is used.

**Formulation 3.1** (Final energy functional with strain-energy density splitting)**.** *Let $p_0, p, \Theta_0, \Theta$ be given with the initial conditions $\boldsymbol{u}_0 = \boldsymbol{u}(x, 0)$ and $\varphi_0 = \varphi(x, 0)$. For the loading increments $n = 1, 2, \ldots, N$, find $\boldsymbol{u} := \boldsymbol{u}^n \in V$ and $\varphi := \varphi^n \in W_{in}$ such that:*

$$\mathcal{E}_\varepsilon(\boldsymbol{u}, \varphi) = \underbrace{\frac{1}{2}\Big(g(\varphi_+)\sigma_\varepsilon^+(\boldsymbol{u}), \varepsilon(\boldsymbol{u})\Big)_\Omega + (\sigma_\varepsilon^-(\boldsymbol{u}), \varepsilon(\boldsymbol{u}))_\Omega}_{\text{Mechanical term}} - \underbrace{\langle \tilde{\tau}, \boldsymbol{u} \rangle_{\Gamma_N}}_{\text{External load}}$$

$$- \underbrace{((\alpha_B - 1)(p - p_0)\varphi_+^2, \nabla \cdot \boldsymbol{u}) + (\nabla(p - p_0)\varphi_+^2, \boldsymbol{u})}_{\text{Pressure term}}$$

$$- \underbrace{((3\alpha_\Theta K_d + C_\Theta)(\Theta - \Theta_0)\varphi_+^2, \nabla \cdot \boldsymbol{u}) + (C_\Theta \nabla(\Theta - \Theta_0)\varphi_+^2, \boldsymbol{u})}_{\text{Thermal term}}$$

$$+ \underbrace{G_c\left(\frac{1}{2\varepsilon}\|1 - \varphi\|^2 + \frac{\varepsilon}{2}\|\nabla\varphi\|^2\right)}_{\text{Fracture term}}.$$

**Remark 3.1.** *In the case of elastic cracks, it can be shown that the phase field unknown satisfies $0 \leq \varphi \leq 1$. In order to establish this property for the spatially continuous incremental problem, we need to modify energy functional for the negative values of $\varphi$. Hence, similar to [35][Section 2], we have used $\varphi_+$ rather than $\varphi$ in terms where negative $\varphi$ could lead to incorrect physics in the bulk energy, traction, pressure and thermal forces.*

**Remark 3.2.** *We briefly mention alternative descriptions for the phase-field approximation and the degradation function. First, using a more general term regarding fracture term is denoted as $\frac{G_c}{4c_w}(\frac{1}{2\varepsilon}W(\varphi) + \frac{\varepsilon}{2}\|\nabla\varphi\|^2)$ for the constant $c_w$ and $W(\varphi)$, which refers to the local part of the dissipated fracture energy functional. This is the so-called `AT-1` fracture model if $c_w = \frac{2}{3}$ and $W(\varphi) = \|1 - \varphi\|$, see [37], and it is `AT-2` for $c_w = \frac{1}{2}$ and $W(\varphi) = \|1 - \varphi\|^2$; see [10]. Second, the quadratic polynomial $g(\varphi)$ can be written in the form of the cubic polynomial as $g(\varphi) := 3(1 - \kappa)\varphi^2 - 2\varphi^3 + \kappa$ or quartic polynomial as $g(\varphi) := 4(1 - \kappa)\varphi^3 - 3\varphi^4 + \kappa$, see [12].*

For $\mathcal{E}_\varepsilon(\boldsymbol{u}, \varphi)$ given in Formulation 3.1, we derive the characterizing Euler-Lagrange equations by differentiating the energy functional with respect to $\boldsymbol{u}$ and $\varphi$:

**Formulation 3.2** (Final Euler-Lagrange equations)**.** *Let $p_0, p, \Theta_0, \Theta$ be given with the initial conditions $\boldsymbol{u}_0 = \boldsymbol{u}(x, 0)$ and $\varphi_0 = \varphi(x, 0)$. For $n = 1, 2, 3, \ldots, N$, find $\boldsymbol{u} := \boldsymbol{u}^n \in V$:*

$$\begin{aligned}
A_1(\boldsymbol{u})(\boldsymbol{w}) = {}& (g(\varphi_+)\sigma_\varepsilon^+(\boldsymbol{u}), \varepsilon(\boldsymbol{w})) + (\sigma_\varepsilon^-(\boldsymbol{u}), \varepsilon(\boldsymbol{w})) - \langle \tilde{\tau}, \boldsymbol{w} \rangle_{\Gamma_N} \\
& - (\alpha_B - 1)((p - p_0)\varphi_+^2, \nabla \cdot \boldsymbol{w}) + (\nabla(p - p_0)\varphi_+^2, \boldsymbol{w}) \\
& - (3\alpha_\Theta K_d + C_\Theta)((\Theta - \Theta_0)\varphi_+^2, \nabla \cdot \boldsymbol{w}) + (C_\Theta \nabla(\Theta_F - \Theta_0)\varphi_+^2, \boldsymbol{w}) = 0 \quad \forall \boldsymbol{w} \in V,
\end{aligned}$$

*and find $\varphi := \varphi^n \in W_{in}$:*

$$\begin{aligned}
A_2(\varphi)(\psi - \varphi) = {}& (1 - \kappa)(\varphi_+ \sigma_\varepsilon^+(\boldsymbol{u}) : \varepsilon(\boldsymbol{u}), \psi - \varphi) \\
& - 2(\alpha_B - 1)(\varphi_+(p - p_0)\nabla \cdot \boldsymbol{u}, \psi - \varphi) + 2(\varphi_+ \nabla(p - p_0)\boldsymbol{u}, \psi - \varphi) \\
& - 2(3\alpha_\Theta K_d + C_\Theta)(\varphi_+(\Theta - \Theta_0)\nabla \cdot \boldsymbol{u}, \psi - \varphi) + 2(C_\Theta \varphi_+ \nabla(\Theta - \Theta_0)\boldsymbol{u}, \psi - \varphi) \\
& + G_c\left(\frac{1}{\varepsilon}(\varphi - 1, \psi - \varphi) + \varepsilon(\nabla\varphi, \nabla(\psi - \varphi))\right) \geq 0 \quad \forall \psi \in W \cap L^\infty.
\end{aligned}$$

### 3.2. The Euler-Lagrange equations in a strong form

In order to complete our derivations, we derive the strong form of Formulation 3.3 in this section. Using integration by parts, we obtain a quasi-stationary elliptic system for the displacements and the phase-field variable, where the latter one is subject to an inequality constraint in time and therefore needs to be complemented with a complementary condition:

**Formulation 3.3** (Strong form of the Euler-Lagrange equations). *Let a pressure $p : \Omega \to \mathbb{R}$ and temperature $\Theta : \Omega \to \mathbb{R}$ and the initial conditions $\boldsymbol{u}_0 = \boldsymbol{u}(x, 0)$ and $\varphi_0 = \varphi(x, 0)$ be given. For the loading steps $n = 1, 2, 3, \ldots, N$, we solve a displacement equation where we seek $\boldsymbol{u} := \boldsymbol{u}^n : \Omega \to \mathbb{R}^d$*

$$
\begin{aligned}
&- \nabla.\left(g(\varphi_+)\sigma_\varepsilon^+(\boldsymbol{u}) + \sigma_\varepsilon^-(\boldsymbol{u})\right) \\
&+ (\alpha_B - 1)\nabla.(\varphi_+^2(p - p_0)) + \varphi_+^2 \nabla(p - p_0) \\
&+ (3\alpha_\Theta K_d + C_\Theta)\nabla.(\varphi_+^2(\Theta - \Theta_0)) + \varphi_+^2 \nabla(\Theta - \Theta_0) = 0 \quad in\ \Omega
\end{aligned}
\tag{21}
$$

$$
\boldsymbol{u} = \boldsymbol{0} \quad on\ \partial\Omega.
\tag{22}
$$

*The phase-field system consists of three parts: the PDE, the inequality constraint, and a compatibility condition (in fracture mechanics called Rice condition [39]). Find $\varphi := \varphi^n : \Omega \to [0, 1]$*

$$
\begin{aligned}
&- \Big(((1 - \kappa)\varphi_+\Psi^+(\boldsymbol{\varepsilon}(\boldsymbol{u})) - G_c\varepsilon\Delta\varphi - \frac{G_c}{\varepsilon}(1 - \varphi) \\
&- 2(\alpha_B - 1)\varphi_+(p - p_0)\nabla \cdot \boldsymbol{u} + 2\varphi_+\nabla(p - p_0)\boldsymbol{u} \\
&- 2(3\alpha_\Theta K_d + C_\Theta)\varphi_+(\Theta - \Theta_0)\nabla \cdot \boldsymbol{u} + 2C_\Theta\varphi_+\nabla(\Theta - \Theta_0)\boldsymbol{u}\Big) \leqslant 0 \quad in\ \Omega
\end{aligned}
\tag{23}
$$

$$
\partial_t\varphi \leqslant 0 \quad in\ \Omega,
\tag{24}
$$

$$
\begin{aligned}
&- \Big(((1 - \kappa)\varphi_+\Psi^+(\boldsymbol{\varepsilon}(\boldsymbol{u})) - G_c\varepsilon\Delta\varphi_+ - \frac{G_c}{\varepsilon}(1 - \varphi_+) \\
&- 2(\alpha_B - 1)\varphi_+(p - p_0)\nabla \cdot \boldsymbol{u} + 2\varphi_+\nabla(p - p_0)\boldsymbol{u} \\
&- 2(3\alpha_\Theta K_d + C_\Theta)\varphi_+(\Theta - \Theta_0)\nabla \cdot \boldsymbol{u} + 2C_\Theta\varphi_+\nabla(\Theta - \Theta_0)\boldsymbol{u}\Big) \partial_t\varphi = 0 \quad in\ \Omega,
\end{aligned}
\tag{25}
$$

$$
\partial_{\boldsymbol{n}}\varphi = 0 \quad on\ \partial\Omega.
\tag{26}
$$

### 3.3. Global balance principle of continuum thermo-mechanics

In this section, thermodynamical consistency for the preservation of the principal of balance of energy is shown by considering a sequence of variational substitutions. As a point of departure, considering Formulation 3.1, we define the total free energy functional as

$$
\begin{aligned}
\mathcal{E}(\boldsymbol{u}, \varphi_+) &:= \mathcal{E}_{bulk}(\boldsymbol{u}, \varphi_+) + \mathcal{E}_{crack}(\varphi) + \mathcal{E}_{ext}(\boldsymbol{u}) \\
&:= \int_\Omega W_{bulk}(\boldsymbol{\varepsilon}(\boldsymbol{u}), \varphi_+) \, \mathrm{d}\mathbf{x} + \int_\Omega W_{crack}(\varphi) \, \mathrm{d}\mathbf{x} - \int_{\Gamma_N} \tilde{\boldsymbol{\tau}} \cdot \boldsymbol{u} \, \mathrm{d}s,
\end{aligned}
\tag{27}
$$

with the bulk free energy functional

$$
\begin{aligned}
W_{bulk}\Big(\boldsymbol{\varepsilon}(\boldsymbol{u}), \varphi_+\Big) :=&\ g(\varphi_+)\Psi^+(\boldsymbol{\varepsilon}(\boldsymbol{u})) + \Psi^-(\boldsymbol{\varepsilon}(\boldsymbol{u})) \\
&- ((\alpha_B - 1)(p - p_0)\varphi_+^2.\nabla \cdot \boldsymbol{u}) + (\nabla(p - p_0)\varphi_+^2.\boldsymbol{u}) \\
&- ((3\alpha_\Theta K_d + C_\Theta)(\Theta - \Theta_0)\varphi_+^2.\nabla \cdot \boldsymbol{u}) + (C_\Theta\nabla(\Theta - \Theta_0)\varphi_+^2.\boldsymbol{u}),
\end{aligned}
\tag{28}
$$

and the crack free energy functional

$$
W_{crack}(\varphi, \nabla\varphi) := G_c\gamma_\varepsilon(\varphi, \nabla\varphi).
\tag{29}
$$

Here, we have introduced the second order crack surface density function per unit volume of the thermo-poroelastic media as,

$$\gamma_\varepsilon(\varphi, \nabla\varphi) := \frac{1}{2\varepsilon}|1 - \varphi|^2 + \frac{\varepsilon}{2}|\nabla\varphi|^2. \tag{30}$$

We recall that weak forms derived for the displacement and phase-field are given in Formulation 3.2. To derive a global balance of energy, we choose as test functions $w =: \dot{u}$ and $\psi =: \dot{\varphi}$ and restate Formulation 3.2 for the mechanical part as,

$$
\begin{aligned}
A_1(\boldsymbol{u})(\dot{\boldsymbol{u}}) =&(g(\varphi_+)\boldsymbol{\sigma}_\varepsilon^+(\boldsymbol{u}), \nabla(\dot{\boldsymbol{u}})) + (\boldsymbol{\sigma}_\varepsilon^-(\boldsymbol{u}), \nabla(\dot{\boldsymbol{u}})) - \langle\tilde{\boldsymbol{\tau}}, \dot{\boldsymbol{u}}\rangle_{\Gamma_N} \\
&- (\alpha_B - 1)((p - p_0)\varphi_+^2, tr(\nabla\dot{\boldsymbol{u}}) + (\nabla(p - p_0)\varphi_+^2, \dot{\boldsymbol{u}}) \\
&- (3\alpha_\Theta K_d + C_\Theta)((\Theta - \Theta_0)\varphi_+^2, tr(\nabla\dot{\boldsymbol{u}})) + (C_\Theta\nabla(\Theta - \Theta_0)\varphi_+^2, \dot{\boldsymbol{u}}) = 0 \quad \forall\dot{\boldsymbol{u}} \in V.
\end{aligned}
\tag{31}
$$

We define the second order displacement gradient denoted as $\boldsymbol{H} := \nabla\boldsymbol{u}$, then Eq. (30) reduces to

$$
\begin{aligned}
A_1(\boldsymbol{u})(\dot{\boldsymbol{u}}) =&(g(\varphi_+)\boldsymbol{\sigma}_\varepsilon^+(\boldsymbol{u}), \dot{\boldsymbol{H}}) + (\boldsymbol{\sigma}_\varepsilon^-(\boldsymbol{u}), \dot{\boldsymbol{H}}) - \langle\tilde{\boldsymbol{\tau}}, \dot{\boldsymbol{u}}\rangle_{\Gamma_N} \\
&- (\alpha_B - 1)((p - p_0)\varphi_+^2, tr(\dot{\boldsymbol{H}}) + (\nabla(p - p_0)\varphi_+^2, \dot{\boldsymbol{u}}) \\
&- (3\alpha_\Theta K_d + C_\Theta)((\Theta - \Theta_0)\varphi_+^2, tr(\dot{\boldsymbol{H}})) + (C_\Theta\nabla(\Theta - \Theta_0)\varphi_+^2, \dot{\boldsymbol{u}}) = 0 \quad \forall\dot{\boldsymbol{u}} \in V,
\end{aligned}
\tag{32}
$$

that is

$$\int_\Omega \dot{W}_{bulk}\left(\boldsymbol{u}, \boldsymbol{\varepsilon}(\boldsymbol{u}), \varphi_+\right) \mathrm{d}\mathbf{x} - \int_\Omega \frac{\partial W_{bulk}}{\partial\varphi}\dot{\varphi}\,\mathrm{d}\mathbf{x} - P^{ext} = 0, \tag{33}$$

$$\Leftrightarrow \qquad P^{int} - \int_\Omega \frac{\partial W_{bulk}}{\partial\varphi}\dot{\varphi}\,\mathrm{d}\mathbf{x} - P^{ext} = 0. \tag{34}$$

Herein, the rate of internal mechanical power which describes the response of a domain $\Omega$ done by the stress field is

$$P^{int} = \int_\Omega \dot{W}_{bulk}\left(\boldsymbol{u}, \boldsymbol{\varepsilon}(\boldsymbol{u}), \varphi_+\right) = \int_\Omega \frac{\partial W_{bulk}}{\partial\boldsymbol{u}}.\dot{\boldsymbol{u}}\,\mathrm{d}\mathbf{x} + \int_\Omega \frac{\partial W_{bulk}}{\partial\boldsymbol{\varepsilon}} : \dot{\boldsymbol{\varepsilon}}\,\mathrm{d}\mathbf{x} + \int_\Omega \frac{\partial W_{bulk}}{\partial\varphi}\dot{\varphi}\,\mathrm{d}\mathbf{x}. \tag{35}$$

Accordingly, through Formulation 3.2 for the phase-field part, we derive

$$A_2(\varphi)(\dot{\varphi}) = \int_\Omega \frac{\partial W_{bulk}}{\partial\varphi}\dot{\varphi}\,\mathrm{d}\mathbf{x} + \int_\Omega G_c\left(\frac{1}{\varepsilon}(\varphi - 1).\dot{\varphi} + \varepsilon(\nabla\varphi)\nabla\dot{\varphi}\right) = 0 \qquad \forall\dot{\varphi} > 0 \in W. \tag{36}$$

It is important to note that the inequality $A_2(\cdot)(\cdot)$ in Formulation 3.2 becomes an equality in Eq. 36 because we consider the situation in which the inequality constraint (24) is strictly fulfilled; namely $\dot{\varphi} < 0$. In this case equality must hold in (23) (and thus in $A_2(\cdot)(\cdot)$) since otherwise the compatibility condition (25) is not fulfilled. We can restate Eq. 36 as follows,

$$\dot{\mathcal{E}}_{crack}(\varphi) = \int_\Omega G_c\delta_\varphi\gamma_\varepsilon(\varphi, \nabla\varphi)\dot{\varphi}\mathrm{d}\mathbf{x} = -\int_\Omega \frac{\partial W_{bulk}}{\partial\varphi}\dot{\varphi}\,\mathrm{d}\mathbf{x}, \tag{37}$$

where the left-hand side is considered to be a functional of the rate of the crack phase-field and that is the global crack dissipation functional, i.e. $\dot{\mathcal{E}}_{crack}(\varphi)$, hence

$$\dot{\mathcal{E}}_{crack}(\varphi) \geqslant 0. \tag{38}$$

Through the second term in Eq. 37 and considering Eq. 38, the local form of crack dissipation reads,

$$\delta_\varphi\gamma_\varepsilon(\varphi, \nabla\varphi) \leqslant 0 \qquad \text{and} \qquad \dot{\varphi} \leqslant 0, \tag{39}$$

and the third term of Eq. 37 leads to the additional local condition, i.e.

11

$$\beta_\varphi := \frac{\partial W_{bulk}(\boldsymbol{u}, \varphi_+)}{\partial \varphi} \geqslant 0. \tag{40}$$

Herein, $\beta_\varphi$ introduced as a crack deriving force is conjugate to the phase-field variable, that is

$$\begin{aligned}
\beta_\varphi = {} & 2(1-\kappa)\varphi_+\Psi(\boldsymbol{\varepsilon}(\boldsymbol{u})) \\
& - 2((\alpha_B - 1)(p - p_0)\varphi_+, \nabla \cdot \boldsymbol{u}) + 2(\nabla(p - p_0)\varphi_+, \boldsymbol{u}) \\
& - 2((3\alpha_\Theta K_d + C_\Theta)(\Theta - \Theta_0)\varphi_+, \nabla \cdot \boldsymbol{u}) + 2(C_\Theta\nabla(\Theta - \Theta_0)\varphi_+, \boldsymbol{u}).
\end{aligned} \tag{41}$$

In our formulation, in comparison to Miehe et al. [31] we have $\beta_\varphi = -f$ (due to the definition of the crack phase-field like the damage variable in the Miehe et al. [31]). Note that $\beta_\varphi$ becomes zero in the fracture surface, i.e. $C$, as $\varphi$ becomes zero.

**Remark 3.3.** *We now look into more detail in the positivity condition for the Eq. 41 and discuss term by term. It is noted due to the condition obtained from Eq. 38 which is the positivity of the global crack dissipation functional, and by considering third term in Eq. 37 leads to the positivity of the crack deriving force, i.e. $\beta_\varphi \geqslant 0$ and $\dot{\varphi} \leqslant 0$, i.e. Eq. 40. Hence, for the evolving fracture, by means of Eq. 41, the first term including $\Psi(\boldsymbol{\varepsilon}(\boldsymbol{u}))$ is positive due to the normalization condition and for the second and fourth terms we are demanding for pressure $p \geqslant p_0$ and thermal $\Theta \leqslant \Theta_0$ both conditions hold (i.e. $\beta_\varphi \geqslant 0$) to satisfy positiveness of the global crack dissipation functional (it is assumed the gradient term for both pressure and thermal part are neglected and $\alpha_B \ll 1$). It has to be noted, due to decoupled strain energy density function we have used (see Section 3.1), results in $\nabla.\boldsymbol{u} > 0$ in $\Omega_F$ (i.e., the transition zone). This can be observed later in Fig. 15 and 18. Additionally, $\dot{\varphi} \leqslant 0$ is imposed to the total energy functional through the primal-dual active set strategy (see Section 4.3). By doing so, the first condition in Eq. 39 is automatically satisfied (due to satisfaction of the third term in Eq. 37. This results in the positivity of the second term in Eq. 37) if and only if both $p \geqslant p_0$ and $\Theta \leqslant \Theta_0$ hold.*

To derive the Karush-Kuhn-Tucker conditions, we consider Eq. 37, and the functional derivative with respect to the $\varphi$ defined as:

$$\int_\Omega \delta_\varphi \gamma_\varepsilon(\varphi, \nabla\varphi)\mathrm{d}\mathbf{x} := \int_\Omega \left(\frac{\partial\gamma}{\partial\varphi} + \frac{\partial\gamma}{\partial\nabla\varphi}\right)\mathrm{d}\mathbf{x} = \int_\Omega \left(\frac{\partial\gamma}{\partial\varphi} - \nabla.[\frac{\partial\gamma}{\partial\nabla\varphi}]\right)\mathrm{d}\mathbf{x}, \tag{42}$$

that is

$$\int_\Omega \delta_\varphi \gamma_\varepsilon(\varphi, \nabla\varphi)\mathrm{d}\mathbf{x} = \int_\Omega \frac{1}{\varepsilon}[(\varphi - 1) - \varepsilon^2\Delta\varphi]\mathrm{d}\mathbf{x}. \tag{43}$$

Due to $\frac{\partial\gamma_\varepsilon(\varphi,\nabla\varphi)}{\partial\nabla\varphi}.\boldsymbol{n} = \varepsilon\nabla\varphi.\boldsymbol{n} = 0$, that is Euler-Lagrange crack phase-field equation on the boundary of the given domain. The right hand side of Eq. 37, i.e. $-\int_\Omega \beta_\varphi \dot{\varphi}\,\mathrm{d}\mathbf{x}$, can also be obtained by means of Eq. 34 and hence Eq. 37 is restated as,

$$\Pi(\dot{\boldsymbol{u}}, \dot{\varphi}) = \dot{\mathcal{E}}_{crack}(\varphi) + P^{int}(\dot{\boldsymbol{u}}, \dot{\varphi}) - P^{ext}(\dot{\boldsymbol{u}}) = 0, \tag{44}$$

that is a global form of the balance of energy for the coupled two-field problem describing the evolution of internal energy and crack dissipation energy, i.e. $\dot{\mathcal{E}}_{crack}(\varphi) + P^{int}$, in a system due to the external loads, i.e. $P^{ext}$. Additionally, by means of the second and the third terms in Eq. 37, it turns out that

$$\int_\Omega (\beta_\varphi + G_c\delta_\varphi\gamma_\varepsilon(\varphi, \nabla\varphi))\dot{\varphi}\mathrm{d}\mathbf{x} = 0, \tag{45}$$

which is the balance law for the evolution of the crack phase-field which ensuring the principal of maximum dissipation during the crack phase-field evolution (see e.g. [31]) and so-called as a compatibility condition;

we refer the reader also to Section 3.2. Observe that one may satisfy this global irreversibility constraint of crack evolution, i.e. Eq. 45 by ensuring locally a positive variational derivative of the crack surface function and a positive evolution of the crack phase field, i.e.

$$\beta_\varphi + G_c \delta_\varphi \gamma_\varepsilon(\varphi, \nabla\varphi) \leqslant 0, \quad \text{and} \quad \dot\varphi \leqslant 0. \tag{46}$$

The former condition is ensured in the subsequent treatment by a constitutive assumption that relates the functional derivative to a positive energetic driving force. The latter constraint is a natural assumption that relates the fracture phase field for the non-reversible evolution of crack phase-field.

**Remark 3.4.** *It is noted within loading state, i.e. $\dot\varphi < 0$, due to the compatibility condition, i.e. Eq. 45, along with Eq. 46, one may observe $\beta_\varphi + G_c \delta_\varphi \gamma_\varepsilon(\varphi, \nabla\varphi) = 0$ and in the unloading state, i.e. $\dot\varphi = 0$, we have $\beta_\varphi + G_c \delta_\varphi \gamma_\varepsilon(\varphi, \nabla\varphi) < 0$. Equation 46 along with Eq. 45 refer to the Karush-Kuhn-Tucker conditions for the phase-field fracturing problem.*

**Remark 3.5.** *It turns out that, if the positivity of the crack deriving force is satisfied (see Remark 3.3), i.e. $\beta_\varphi \geqslant 0$, and according to Eq. 46 we have $G_c \delta_\varphi \gamma_\varepsilon(\varphi, \nabla\varphi) \leqslant -\beta_\varphi$ and hence results to $\delta_\varphi \gamma_\varepsilon(\varphi, \nabla\varphi) \leqslant 0$, that is the first inequality condition shown in Eq. 39.*

## 4. Numerical solution and the final discrete model

In this section, we briefly describe spatial discretization first. The solution algorithm is then based on a quasi-monolithic approach for which a Newton solver is employed as described in [24]. The crack irreversibility condition in Eq. 4 is treated with a primal-dual active set method. Both techniques can be gathered into one single combined Newton solver [24, 29, 25].

### 4.1. Spatial discretization

The computational domain is subdivided into quadrilateral or hexahedral element domains. Both subproblems are discretized with a Galerkin finite element method using $H^1$-conforming bilinear (2D) or trilinear (3D) elements, i.e., the ansatz and test space uses $Q_1^c$-finite elements, e.g., for details, we refer readers to the [14]. Consequently, the discrete spaces have the property $V_h \subset V$ and $W_h \subset W$.

### 4.2. Problem statement of the compact minimization problem

The starting point for the discrete solution is Formulation 3.1, written in compact form as:

$$\min_{\boldsymbol{u} \in V, \varphi \in W_{in}} \mathcal{E}_\varepsilon(\boldsymbol{u}, \varphi),$$

For the following, we set $U = (\boldsymbol{u}, \varphi) \in V \times W$. Discretizing

$$\partial_t \varphi \approx \frac{\varphi^{n+1} - \varphi^n}{\delta t},$$

with the time step size $\delta t := t^{n+1} - t^n$, the incremental problem can be rewritten as

$$\min \mathcal{E}_\varepsilon(U)$$
$$\text{subject to } U \leq U^{old} \text{ on } \Phi, \tag{47}$$

where $\Phi = 0 \times W$, so that the constraint acts on the phase-field variable only, and $U^{old}$ is the solution from the last time-step (or the initial condition). The minimization of (47) is numerically challenging, due to the following reasons:

13

1. the energy functional $\mathcal{E}_\varepsilon(\boldsymbol{u}, \varphi)$ may admit several local minimizers. Thus finding the global minimum is in general non-feasible, e.g., [9] for discussions on the pure elasticity case. The existence of a minimizer for pressurized fractures was established in [35]. Since the temperature is a given quantity, as the pressure, the proof for existence of the current $\mathcal{E}_\varepsilon(\boldsymbol{u}, \varphi)$ goes along the same lines as in [9],

2. the irreversibility of crack phase-field, i.e. $|C_{t-1}| \leq |C_t|$, is required to provide a thermodynamically consistent minimization problem by having a positive crack dissipation inequality and enforcing on the temporal derivative of the phase-field function, see e.g. [33],

3. the minimization problem is characterized by localization of the crack phase-field in bands of width of order $\varepsilon$. From a practical and numerical analysis point of view, $\varepsilon > h$ must hold (at least one element has to be existed to cover regularized phased-field). In more detail, $h = o(\varepsilon)$. The regularization parameter is typically a very small dimensionless value and for the accurate fracture response (i.e. converge toward the sharp crack profile) which should tend to 0 in the limit $h \to 0$ to resolve the bands, see e.g. [20],

4. the linear system of equations arises from Hessian matrix of the $\mathcal{E}_\varepsilon(\boldsymbol{u}, \varphi)$ are typically badly conditioned due to the presence of crack phase-field localizations band where the elastic stiffness varies rapidly from the intact value to zero, see e.g. [17].

*4.3. A combined Newton method: treating crack irreversibility and solving the nonlinear problem*

In following, we will address how to resolve the issues mentioned above. To this end, we first describe Newton's method for solving the unconstrained minimization problem $\min \mathcal{E}_\varepsilon(\boldsymbol{U})$ in Eq. 47 for the total energy functional $\mathcal{E}_\varepsilon(\boldsymbol{U})$ given in formulation 3.1. We construct a sequence $\boldsymbol{U}^0, \boldsymbol{U}^1, \ldots, \boldsymbol{U}^N$ with

$$\boldsymbol{U}^{k+1} = \boldsymbol{U}^k + \delta \boldsymbol{U}^k,$$

where the update $\delta \boldsymbol{U}^k$ is computed as the solution of the linear system (details in Section 4.4):

$$\nabla^2 \mathcal{E}_\varepsilon(\boldsymbol{U}^k)\, \delta \boldsymbol{U}^k = -\nabla \mathcal{E}_\varepsilon(\boldsymbol{U}^k). \tag{48}$$

If we assume the constraints on the phase-field on Eq. 47 hold for the initial guess $\boldsymbol{U}^0$ (we will start with the solution from the last time step, which satisfies the constraint), the condition

$$\delta \boldsymbol{U}^k \leq \boldsymbol{0} \text{ on } \Phi, \tag{49}$$

implies that $\boldsymbol{U}^{k+1} = \boldsymbol{U}^k + \delta \boldsymbol{U}^k \leq \boldsymbol{U}^k \leq \cdots \leq \boldsymbol{U}^0 \leq \boldsymbol{U}^{old}$ on $\Phi$. In a variational formulation, the previous Newton method reads:

$$\nabla^2 \mathcal{E}_\varepsilon(\boldsymbol{U}_h^k)(\delta \boldsymbol{U}_h^k, \boldsymbol{\Psi}) = -\nabla \mathcal{E}_\varepsilon(\boldsymbol{U}_h^k)(\boldsymbol{\Psi}), \quad \forall \boldsymbol{\Psi} \in V_h \times W_h, \quad \text{with} \quad \delta \boldsymbol{U}^k \leq 0 \text{ on } \Phi, \tag{50}$$

where $\boldsymbol{\Psi} := [\boldsymbol{w}, \psi]$ is denoted as the total test function. Crack irreversibility is taken care of by removing the corresponding rows and columns in which the constraint is is active. This yields then a reduced system. In our implementation, we combine two Newton methods (active set and the nonlinear iteration for the PDE solution; see Section 4.4) into a single update loop with variable $\delta \boldsymbol{U}^k$. This Newton loop contains a backtracking line search to improve the convergence radius. This yields Algorithm 1.

**Remark 4.1** (Stopping criteria)**.** *We remark that the above algorithm has two stopping criteria that must be achieved simultaneously:*

$$\mathcal{A}_{k+1} = \mathcal{A}_k \qquad and \qquad \widetilde{\boldsymbol{R}}(\boldsymbol{U}_h^k) < TOL_{N-R}\, \widetilde{\boldsymbol{R}}(\boldsymbol{U}_h^0). \tag{51}$$

**Remark 4.2.** *It is important to distinguish between the full residual $\boldsymbol{R}(\boldsymbol{U}_h^k)$ and $\widetilde{\boldsymbol{R}}(\boldsymbol{U}_h^k)$. The latter is the residual on the inactive set, which can be computed by eliminating the active set constraints from the former.*

**Input**: loading data $(u, \varphi, p_t, p_0, \Theta, \Theta_0, t)$ on $\Gamma_D, \Gamma_N \subset \partial\Omega$;

solution $U_{n-1} := (u_{n-1}, \varphi_{n-1})$ from time step $n - 1$.

Combined Newton / primal-dual active set iteration $k \geq 1$:
- Assemble residual $R(U_h^k)$,
- Compute active set $\mathcal{A}_k = \{i \mid (B^{-1})_{ii}(R_k)_i + c(\delta U_h^k)_i > 0\}$,
- Assemble matrix $G = \nabla^2 E_\varepsilon(U_h^k)$ and right-hand side $F = -\nabla E_\varepsilon(U_h^k)$,
- Eliminate rows and columns in $\mathcal{A}_k$ from $G$ and $F$ to obtain $\widetilde{G}$ and $\widetilde{F}$,
- Solve linear system $\widetilde{G}\delta U_k = \widetilde{F}$, i.e. find $\delta U_h^k \in V_h \times W_h$ with,
$$\nabla^2 \mathcal{E}_\varepsilon(U_h^k)(\delta U_h^k, \Psi) = -\nabla \mathcal{E}_\varepsilon(U_h^k)(\Psi), \quad \forall \Psi \in V_h \times W_h,$$
where $\nabla^2 \mathcal{E}_\varepsilon$ and $\nabla \mathcal{E}_\varepsilon$ are defined in Section 4.4 and 4.5.
- Find a step size $0 < \omega \leq 1$ using back-tracking line search algorithm to get
$$U_h^{k+1} = U_h^k + \omega \delta U_h^k \text{ with } \widetilde{R}(U_h^{k+1}) < \widetilde{R}(U_h^k).$$
- if fulfilled, such that
$$\mathcal{A}_{k+1} = \mathcal{A}_k \text{ and } \widetilde{R}(U_h^k) < \mathtt{TOL_{N-R}} \, \widetilde{R}(U_h^0)$$
set $(u^k, \varphi^k) =: (u_t, \varphi_t)$ and stop;
else $k + 1 \to k$.

**Output:** solution $(u_n, \varphi_n) =: U_n$.

### 4.4. On the Jacobian and the residual inside Newton's method

For solving the PDE problem at each Newton step, we focus on a monolithic scheme in which all equations are solved simultaneously resulting in one semi-linear form. However, it is well known that the energy functional (3) is not convex simultaneously in both solution variables $u$ and $\varphi$; but separately in each variable while keeping the other fixed. Consequently, solving the Euler-Lagrange equations in a straightforward way is not possible and influences the robustness and efficiency of the solution scheme because of an (possibly) indefinite Hessian matrix $G$ [19, 48, 49].

The critical terms arise in the Hessian matrix $G$, are the cross terms, includes for mechanical term i.e. $\left(((1 - \kappa)\varphi_+^2 + \kappa)\sigma_\varepsilon^+(u), \varepsilon(w)\right)$, for pressure term i.e. $(\alpha_B - 1)((p - p_0)\varphi_+^2, \nabla \cdot w)$, $(\nabla(p - p_0)\varphi_+^2, w)$ and for thermal term i.e. $(3\alpha_\Theta K + C_\Theta)((\Theta - \Theta_0)\varphi_+^2, \nabla \cdot w)$ and $(C_\Theta \nabla(\Theta - \Theta_0)\varphi^2, w)$. To this end, according to [24], for having a convex energy functional, $A_1$ is linearized in the direction of the $u$ and $\varphi$ by linear extrapolation and time-lagging of the phase-field, i.e. $\varphi \approx \tilde{\varphi} := \varphi(\varphi^{n-2}, \varphi^{n-1})$ in order to obtain a convex energy functional, that is

$$\tilde{\varphi} := \varphi(\varphi^{n-2}, \varphi^{n-1}) = \varphi^{n-2} \frac{t^n - t^{n-1}}{t^{n-2} - t^{n-1}} + \varphi^{n-1} \frac{t^n - t^{n-2}}{t^{n-1} - t^{n-2}}. \tag{52}$$

Here, $\varphi^{n-2}, \varphi^{n-1}$ denote the solutions to previous time steps, denoted as $t^{n-2}$ and $t^{n-1}$, see Fig. 2.

Hence, linearization of $A_1(u)(w)$ (see Formulation 3.2) in the direction of $\varphi$, i.e. $\delta\varphi$, within tangent stiffness matrix (the Hessian matrix) is neglected (due to the given $\tilde{\varphi}$).

In the following, we state monolithic formulations for the displacement-phase-field system. The presentation is similar to [24]. Specifically, the phase-field variable is time-lagged in the first term of the displacement equation. For fully monolithic solution algorithms and their performance we refer the reader to [48, 49, 19]. In the following, we deal with equalities since we removed the inequality constraint via the primal-dual active
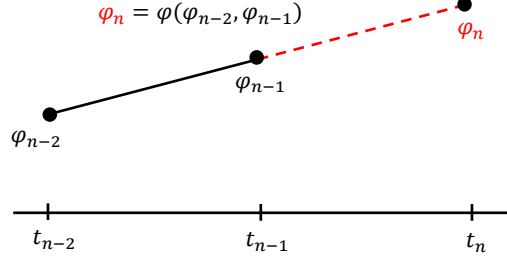
Figure 2: Linear extrapolation in time for the $\varphi$ based on two previous solutions, i.e. $\varphi^{n-2}, \varphi^{n-1}$.

set strategy. The residual reads:

$$
\begin{aligned}
A(\boldsymbol{U})(\boldsymbol{\Psi}) := \nabla \mathcal{E}_\varepsilon(\boldsymbol{U})(\boldsymbol{\Psi}) = {} & (g(\tilde{\varphi}_+)\sigma_\varepsilon^+(\boldsymbol{u}), \boldsymbol{\varepsilon}(\boldsymbol{w})) + (\sigma_\varepsilon^-(\boldsymbol{u}), \boldsymbol{\varepsilon}(\boldsymbol{w})) - \langle \tilde{\boldsymbol{\tau}}, \boldsymbol{w} \rangle_{\Gamma_N} \\
& - (\alpha_B - 1)((p - p_0)\tilde{\varphi}_+^2, \nabla \cdot \boldsymbol{w}) + (\nabla(p - p_0)\tilde{\varphi}_+^2, \boldsymbol{w}) \\
& - (3\alpha_\Theta K_d + C_\Theta)((\Theta - \Theta_0)\tilde{\varphi}_+^2, \nabla \cdot \boldsymbol{w}) + (C_\Theta \nabla(\Theta - \Theta_0)\tilde{\varphi}_+^2, \boldsymbol{w}) \\
& + (1 - \kappa)(\varphi_+ \sigma_\varepsilon^+(\boldsymbol{u}) : \boldsymbol{\varepsilon}(\boldsymbol{u}), \psi) \\
& - 2(\alpha_B - 1)((p - p_0)\nabla \cdot \boldsymbol{u}\, \varphi_+, \psi) + 2(\nabla(p - p_0)\boldsymbol{u}\, \varphi_+, \psi) \\
& - 2(3\alpha_\Theta K_d + C_\Theta)((\Theta - \Theta_0)\nabla \cdot \boldsymbol{u}\, \varphi_+, \psi) + 2(C_\Theta \nabla(\Theta - \Theta_0)\boldsymbol{u}\, \varphi_+, \psi) \\
& + G_c\left(\frac{1}{\varepsilon}(\varphi - 1, \psi) + \varepsilon(\nabla\varphi, \nabla\psi)\right).
\end{aligned}
\tag{53}
$$

The corresponding Jacobian is built by computing the directional derivative $A'(\boldsymbol{U})(\delta\boldsymbol{U}, \boldsymbol{\Psi})$. Then:

$$
\begin{aligned}
A'(\boldsymbol{U})(\delta\boldsymbol{U}, \boldsymbol{\Psi}) : = {} & \nabla^2 \mathcal{E}_\varepsilon(\boldsymbol{U})(\delta\boldsymbol{U}, \boldsymbol{\Psi}) \\
= {} & \left(g(\tilde{\varphi}_+)\,\sigma_\varepsilon^+(\delta\boldsymbol{u}), \boldsymbol{\varepsilon}(\boldsymbol{w})\right) + (\sigma_\varepsilon^-(\delta\boldsymbol{u}), \boldsymbol{\varepsilon}(\boldsymbol{w})) \\
& + (1 - \kappa)\left(\delta\varphi_+ \sigma^+(\boldsymbol{u}) : \boldsymbol{\varepsilon}(\boldsymbol{u}) + \varphi_+\, \sigma_\varepsilon^+(\delta\boldsymbol{u}) : \boldsymbol{\varepsilon}(\boldsymbol{u}) + \varphi_+\, \sigma_\varepsilon^+(\boldsymbol{u}) : \boldsymbol{\varepsilon}(\delta u), \psi\right) \\
& - 2(\alpha_B - 1)(p - p_0)(\delta\varphi_+ \mathrm{div}\, \boldsymbol{u} + \varphi_+\, \mathrm{div}\, \delta\boldsymbol{u}, \psi) \\
& + 2\nabla(p - p_0)(\delta\varphi \boldsymbol{u} + \varphi_+\, \delta\boldsymbol{u}, \psi) \\
& - 2(3\alpha_\Theta K_d + C_\Theta)(\Theta - \Theta_0)(\delta\varphi \mathrm{div}\, \boldsymbol{u} + \varphi_+\, \mathrm{div}\, \delta\boldsymbol{u}, \psi) \\
& + 2C_\Theta \nabla(\Theta - \Theta_0)(\delta\varphi \boldsymbol{u} + \varphi_+\, \delta\boldsymbol{u}, \psi) \\
& + G_c\left(\frac{1}{\varepsilon}(\delta\varphi, \psi) + \varepsilon(\nabla\delta\varphi, \nabla\psi)\right).
\end{aligned}
\tag{54}
$$

### 4.5. On the linear equation system at each Newton step

#### 4.5.1. Spatial discretization and block structure

In this section, we consider the structure and solution of the linear discrete system (50) arising in each Newton step. For spatial discretization, we use the previously introduced spaces $V_h \times W_h$ with vector-valued basis

$$
\{\psi_i \,|\, i = 1, \ldots, N_s\},
$$

16

where the basis functions are primitive (they are only non-zero in one component), so we can separate them into displacement and phase-field basis functions and sort them accordingly:

$$\psi_i = \begin{pmatrix} \chi_i^{\boldsymbol{u}} \\ 0 \end{pmatrix}, \text{ for } i = 1, \ldots, N_u,$$

$$\psi_{(N_{\boldsymbol{u}}+i)} = \begin{pmatrix} 0 \\ \chi_i^{\varphi} \end{pmatrix}, \text{ for } i = 1, \ldots, N_{\varphi},$$

where $N_{\boldsymbol{u}} + N_{\varphi} = N_s$. This is now used to transform (50) into a system of the form

$$\boldsymbol{M}\boldsymbol{x} = \boldsymbol{F}, \tag{55}$$

where $\boldsymbol{M}$ is a block matrix (the Jacobian) and $F$ the right-hand side consisting of the residuals. The block structure is

$$\boldsymbol{M} = \begin{pmatrix} \boldsymbol{M}^{uu} & \boldsymbol{M}^{u\varphi} \\ \boldsymbol{M}^{\varphi u} & \boldsymbol{M}^{\varphi\varphi} \end{pmatrix}, \qquad \boldsymbol{F} = \begin{pmatrix} F^{\boldsymbol{u}} \\ F^{\varphi} \end{pmatrix},$$

with entries coming from (54):

$$\boldsymbol{M}_{i,j}^{uu} = \left( \left( (1-\kappa)\tilde{\varphi}_+^2 + \kappa \right) \boldsymbol{\sigma}_{\varepsilon}^+(\chi_j^{\boldsymbol{u}}), \boldsymbol{\varepsilon}(\chi_i^{\boldsymbol{u}}) \right) + (\boldsymbol{\sigma}_{\varepsilon}^-(\chi_j^{\boldsymbol{u}}), \boldsymbol{\varepsilon}(\chi_i^{\boldsymbol{u}})),$$

$$\boldsymbol{M}_{i,j}^{\varphi u} = 2(1-\kappa)(\varphi_+ \, \boldsymbol{\sigma}_{\varepsilon}^+(\chi_j^{\boldsymbol{u}}) : \boldsymbol{\varepsilon}(\boldsymbol{u}), \chi_i^{\varphi})$$

$$\qquad - 2(\alpha_E - 1)(p - p_0)(\varphi_+ \, \nabla.(\chi_j^{\boldsymbol{u}}), \chi_i^{\varphi})$$

$$\qquad + 2\nabla(p - p0)\varphi_+ \, (\chi_j^{\boldsymbol{u}}, \chi_i^{\varphi})$$

$$\qquad - 2(3\alpha_\Theta K_d + C_\Theta)((\Theta - \Theta_0)(\varphi_+ \, \nabla.(\chi_j^{\boldsymbol{u}}), \chi_i^{\varphi})$$

$$\qquad + 2C_\Theta \nabla(\Theta - \Theta_0)\varphi_+ \, (\chi_j^{\boldsymbol{u}}, \chi_i^{\varphi}),$$

$$\boldsymbol{M}_{i,j}^{u\varphi} = 0, \tag{56}$$

$$\boldsymbol{M}_{i,j}^{\varphi\varphi} = (1-\kappa)(\boldsymbol{\sigma}_{\varepsilon}^+(\boldsymbol{u}) : \boldsymbol{\varepsilon}(\boldsymbol{u})\chi_j^{\varphi}, \chi_i^{\varphi})$$

$$\qquad - 2(\alpha_B - 1)(p - p_0)(\nabla.(\boldsymbol{u})\chi_j^{\varphi}, \chi_i^{\varphi})$$

$$\qquad - 2(3\alpha_\Theta K_d + C_\Theta)((\Theta - \Theta_0)(\nabla.(\boldsymbol{u})\chi_j^{\varphi}, \chi_i^{\varphi})$$

$$\qquad + 2\boldsymbol{u}\nabla(p - p_0)(\chi_j^{\varphi}, \chi_i^{\varphi})$$

$$\qquad + 2\boldsymbol{u}C_\Theta \nabla(\Theta - \Theta_0)(\chi_j^{\varphi}, \chi_i^{\varphi})$$

$$\qquad + G_c \left( \frac{1}{\varepsilon}(\chi_j^{\varphi}, \chi_i^{\varphi}) + \varepsilon(\nabla\chi_j^{\varphi}, \nabla\chi_i^{\varphi}) \right).$$

**Remark 4.3.** *Since we replaced $\varphi^2$ by $\tilde{\varphi}^2$ in the displacement equation, the block $M_{i,j}^{u\varphi}$ is zero and the Hessian matrix $\boldsymbol{G}$ has triangular structure. In the other case, all blocks would be nonzero; see [48, 49].*

The right-hand side consists of the corresponding residuals (see semi-linear form (53)).

In particular, we have

$$
\begin{aligned}
\boldsymbol{F}_i^{\boldsymbol{u}} &= -\widetilde{A}(\boldsymbol{U}_k)(\chi_i^{\boldsymbol{u}}) \\
&= \left( \left( (1-\kappa)\tilde{\varphi}_{+k}^2 + \kappa \right) \boldsymbol{\sigma}_{\varepsilon}^+(\boldsymbol{u}_k), \boldsymbol{\varepsilon}(\chi_i^{\boldsymbol{u}}) \right) + (\boldsymbol{\sigma}_{\varepsilon}^-(\boldsymbol{u}_k), \boldsymbol{\varepsilon}(\chi_i^{\boldsymbol{u}})) - \langle \tilde{\boldsymbol{\tau}}, \chi_i^{\boldsymbol{u}} \rangle_{\Gamma_N} \\
&\quad - (\alpha_B - 1)(\tilde{\varphi}_{+k}^2(p - p_0), \nabla.\chi_i^{\boldsymbol{u}}) + (\nabla(p - p_0)\tilde{\varphi}_{+k}^2, \chi_i^{\boldsymbol{u}}) \\
&\quad - (3\alpha_\Theta K_d + C_\Theta)(\tilde{\varphi}_{+k}^2(\Theta - \Theta_0), \nabla.\chi_i^{\boldsymbol{u}}) + C_\Theta(\nabla(\Theta - \Theta_0)\tilde{\varphi}_{+k}^2, \chi_i^{\boldsymbol{u}}),
\end{aligned}
$$

$$
\tag{57}
$$

$$
\begin{aligned}
\boldsymbol{F}_i^{\varphi} &= -\widetilde{A}(\boldsymbol{U}_k)(\chi_i^{\varphi}) \\
&= (1-\kappa)(\varphi_{+k}\, \boldsymbol{\sigma}_{\varepsilon}^+(\boldsymbol{u}_k) : \boldsymbol{\varepsilon}(\boldsymbol{u}_k), \chi_i^{\varphi}) \\
&\quad - 2(\alpha_B - 1)(\varphi_k\,(p - p_0)\, \nabla.\boldsymbol{u}_k, \chi_i^{\varphi}) + 2(\varphi_{+k}\, \nabla(p - p_0)\, \boldsymbol{u}_{+k}, \chi_i^{\varphi}) \\
&\quad - 2(3\alpha_\Theta K_d + C_\Theta)(\varphi_{+k}\,(\Theta - \Theta_0)\, \nabla.\boldsymbol{u}_k, \chi_i^{\varphi}) + 2(C_\Theta \varphi_{+k}\, \nabla(\Theta - \Theta_0)\, \boldsymbol{u}_k, \chi_i^{\varphi}) \\
&\quad + G_c\left( -\frac{1}{\varepsilon}(1 - \varphi_k, \chi_i^{\varphi}) + \varepsilon(\nabla\varphi_k, \nabla\chi_i^{\varphi}) \right).
\end{aligned}
$$

The criterion for convergence of the Newton method is based on the relative residual norm that is, $\texttt{Residual} : \|\boldsymbol{F}(\boldsymbol{x}_{k+1})\| \le \texttt{Tol}_{\texttt{N-R}}\|\boldsymbol{F}(\boldsymbol{x}_k)\|$ for the user-prescribed $\texttt{Tol}_{\texttt{N-R}}$.

In the matrix, the degrees of freedom that belong to Dirichlet conditions (here only displacements since we assume Neumann conditions for the phase-field) are strongly enforced by replacing the corresponding rows and columns as usual in a finite element code. In a similar fashion, the rows and columns that belong to nodes of the active set are removed from the matrix. Corresponding right-hand side values in the vector $F$ are set to zero; see as well Table 1.

*4.5.2. Solution of the linear equation systems*

The linear system arising at each Newton step is solved iteratively using a generalized minimal residual (GMRES) scheme with a block diagonal preconditioner, i.e. $\boldsymbol{P}^{-1}$, as follows

$$
\begin{pmatrix} \boldsymbol{M}^{uu} & \boldsymbol{0} \\ \boldsymbol{M}^{\varphi u} & \boldsymbol{M}^{\varphi\varphi} \end{pmatrix} \begin{pmatrix} F^u \\ F^\varphi \end{pmatrix} = \begin{pmatrix} \delta u \\ \delta \varphi \end{pmatrix} \quad \text{with} \quad \boldsymbol{P}^{-1} := \begin{pmatrix} \left( \tilde{\boldsymbol{M}}^{uu} \right)^{-1} & \boldsymbol{0} \\ \boldsymbol{0} & \left( \tilde{\boldsymbol{M}}^{\varphi\varphi} \right)^{-1} \end{pmatrix},
$$

where we approximate the blocks using a single V-cycle of algebraic multigrid (by Trilinos ML, [26]), and due to the in-dependency to the mesh element size, the whole solver scheme is nearly optimal as recently demonstrated for pressurized phase-field fractures in [25]. The main reason why this solver works nicely is that the block-diagonal terms are of elliptic type.

## 5. Numerical studies

The performance of the proposed model is investigated by means of a series of representative numerical examples in two- and three spatial dimensions. The proposed formulation is considered to be a canonically consistent and robust scheme for treating pressurized fractures and non-isothermal setting in thermo-poroelastic media. The emphasis is on verifications of the programming code against analytical solutions obtained with Sneddon-Lowengrub's formula [44] (extended to non-isothermal configurations in [45]) and using realistic material properties. Mesh refinement studies are provided to study the accuracy of our approach. Investigations of the effects strain-energy splitting and solver outcomes are studied in addition. The implementation is based on deal.II [5, 6] and specifically on the programming code from [25].
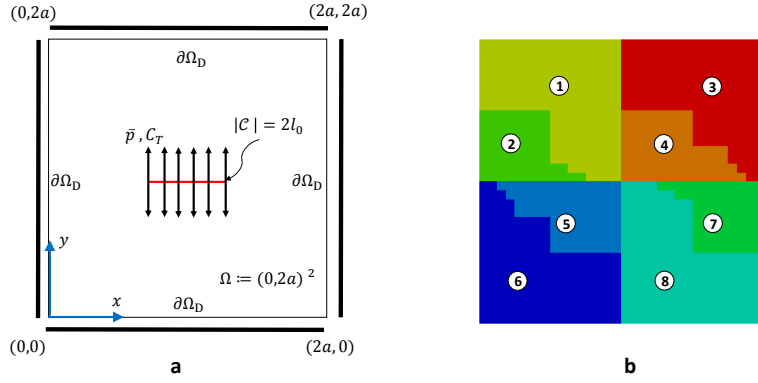
Figure 3: (a) Geometry and loading setup for the 2D test scenarios; (b) All numerical examples are computed by parallel computing on 8 processors. The different subdomains are associated with different processors. Depending on mesh refinement, the workload for each processor is adjusted dynamically at each time step.

## 5.1. Geometries and parameters

### 5.1.1. Two-dimensional setup

In the first five examples, we present two-dimensional settings. The geometrical parameter denoted as $a$ in Fig. 3 is set to 100, and, hence a reservoir of size is $(0, 200)^2$ $m$. The Tran et al. problem is considered in an infinite domain with $C$ with a pre-defined crack of length $2l_0$ in the $y = a$ plane and is restricted in $a - l_0 \leq |C| \leq a + l_0$. We set the half crack length as a $l_0 = 10$ $m$. We set the initial values for displacement and phase-field as $\boldsymbol{u}_0 := 0 \in \Omega$ and $\varphi_0 := 1 \in \Omega_R$ and $\varphi_0 := 0 \in \Omega_F$. The (finite) computational domain is subdivided into quadrilateral element domains. It is noted, that all numerical examples are computed by parallel computing on 8 processors; see Fig. 3[b]. The different sub-domains are associated with different processors. Depending on mesh refinement, the workload for each processor is adjusted dynamically at each time step. Typically, we set $2 \times 10^4$ quadrilateral elements for each processor.
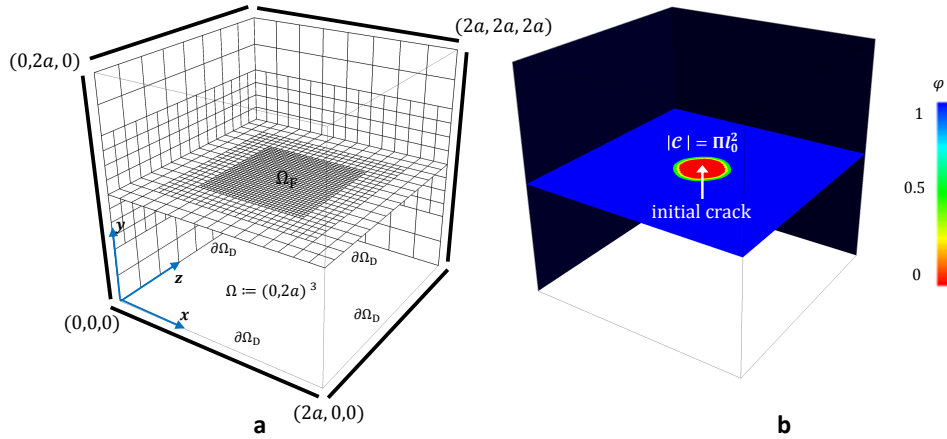


Figure 4: Geometry and initial fracture for the 3D test scenarios. (a) locally refined mesh and (b) initial penny-shape crack in the middle.

### 5.1.2. Three-dimensional setup

In the last two examples, we present three-dimensional test cases. The configuration setup is displayed in Fig. 4 and the values of the material parameters are the same as in the two-dimensional test cases. The geometrical parameter denoted as $a$ in Fig. 4 is set to 50, hence, the reservoir of size is a $(0, 100)^3$ $m$ cube. We consider an infinite domain with $C$ as a pre-defined crack with a given radius $l_0$ in the $y = a$ plane and is

19

restricted in $C(x, y) := \{(x, y) \in \Omega : (x - a)^2 + (z - a)^2 \leq l_0^2\}$. We set the crack radius length as a $l_0 = 10\ m$. The (finite) computational domain is subdivided into hexahedral element domains.

### 5.1.3. Material parameters

The material parameters are taken from [45] and related to practical field problems. The geo-mechanical parameters are Young's modulus $E_Y = 1.5 \times 10^{10} Pa$, Poisson's ratio $\nu = 0.15$, and the linear thermal-expansion coefficient $\beta = 10^{-5} 1/C$ and finally the critical energy release rate $G_c = 10^{10}\ N/m$.

For the flow and temperature, we have the thermal diffusivity $\kappa_\Theta = 10^{-6} m^2/s$, the initial stress $p_0 = 12130$ KPa and in the stationary-in-length test cases (only evolution of the aperture), we use the constant pressure $\bar{p} = 15834$ KPa. Additionally, for the non-isothermal setting, the initial temperature $\Theta_0 = 100\ C$, the apparent temperature is set to $\Theta = 70\ C$.

For all examples, we set $\alpha_B = 0$ and $\alpha_\Theta = 0$. All material properties are fixed for the following numerical examples, unless indicated otherwise.

### 5.1.4. Model parameters

The phase-field parameters are chosen as $\kappa = 10^{-10}$, and $\varepsilon = 10 \times \sqrt{h}$ (respecting the condition $h < \varepsilon$) in 2D and $\varepsilon = 2h$ in the 3D test cases. Using the adaptive mesh refinement, we are not dealing with a uniform mesh and hence the domain is divided into coarser and finer mesh elements, i.e. $\Omega = \Omega_c \cup \Omega_f$. Let $h_c^{max} := max(h_c)$ in $\Omega_c$ and $h_f^{min} := min(h_f)$ in $\Omega_f$. On the one hand $\varepsilon$, enters in the constitutive modeling (that is in our PDE). On the other hand, it implicitly depends on the discretization of a domain, i.e. $h_c^{max} = o(\varepsilon_c)$ and $h_f^{min} = o(\varepsilon_f)$. Thus we define, $\varepsilon := max(\varepsilon_c, \varepsilon_f)$ resulting in $\varepsilon \geqslant h_c > h_f$ and thus $\varepsilon > h$ holds in every point of the domain.

The stopping criterion of the Newton method, i.e. the relative residual norm that is `Residual` $: \|F(x_{k+1})\| \leq$ `Tol`$_{\text{N-R}}\|F(x_k)\|$, is set to `Tol`$_{\text{N-R}} = 10^{-10}$.

The threshold value for the local predictor-corrector mesh refinement is `TOL`$_\varphi = 0.9$. That is, we refine when

$$\varphi(x) < \text{TOL}_\varphi \quad \text{for } x \in \Omega.$$

### 5.2. Test scenarios

We propose the following numerical tests:

- **Case a**. Two-dimensional problem with constant pressure and without thermal effects.

- **Case b**. Two-dimensional problem with constant pressure and fixed Hagoorts decline constant value. That is time-independent problem and considered to validate proposed formulation for fixed thermal effect.

- **Case c**. Two-dimensional problem with constant pressure and evolving Hagoorts decline constant through time. That is a time-dependent problem and used to validate proposed formulation for a temperature variation in time.

- **Case d**. Observing crack propagation in the two-dimensional problem, higher temperature difference is considered. That is time-dependent problem with a constant pressure and evolving Hagoorts decline constant through the time.

- **Case e**. Observing crack propagation in the two-dimensional problem, evolving in time for pressure and Hagoorts decline constant are considered. This is a time-dependent problem.

- **Case f**. Three-dimensional problem with constant pressure and a fixed Hagoorts decline constant value.

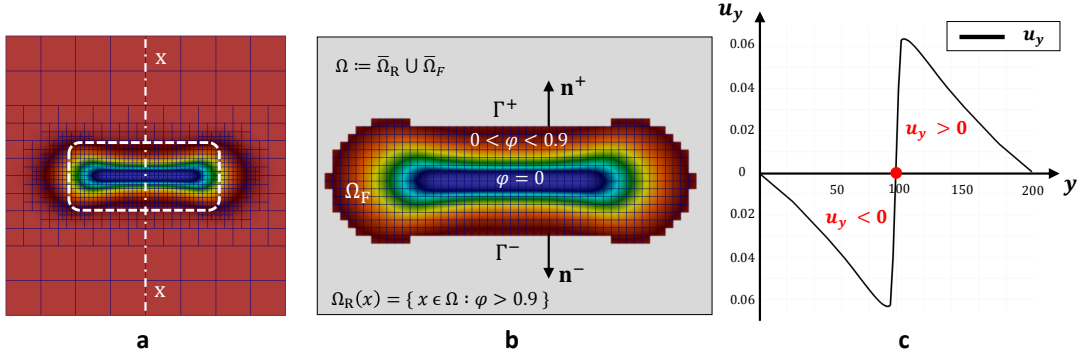- **Case g**. Three-dimensional problem with increasing pressure and Hagoorts decline constant are considered.

Figure 5: (a) Crack phase-field resolution (b) zoom into the framed region of the left plot and that is $\Omega_F := \{x \in \Omega : \varphi(x,t) < 0.9\}$ (c) Profile of the vertical deformation $\boldsymbol{u}_y$ on the section $x - x$ shown in (a) which shows symmetric displacements at the fracture boundary.

### 5.3. Quantities of interest

In our numerical tests, we study the following aspects:

- Crack opening displacements (COD, also known as aperture) for the first three cases:

$$COD := \int_0^{2a} [\boldsymbol{u}^+ \boldsymbol{n}^+] - \int_0^{2a} [\boldsymbol{u}^- \boldsymbol{n}^-] \, dy = \int_0^{2a} [\boldsymbol{u}^+ + \boldsymbol{u}^-].\boldsymbol{n} \, dy = \int_0^{2a} \boldsymbol{u}(x_0, y) \cdot \nabla \varphi(x_0, y) \, dy, \qquad (58)$$

where $\boldsymbol{n} := \boldsymbol{n}^+ = -\boldsymbol{n}^-$ is the normal vector (see Fig. 5 b) and $x_0$ the $x$-coordinate of the integration line. We note that the integration is perpendicular to the crack direction. Here, the crack is aligned with the $x$-axis and therefore integration into the normal direction coincides with the $y$-direction. The analytical solution for the COD derived by Tran et al. [45] reads:

$$w(x,t) = \frac{2(1 - \nu_s^2)l_0}{E} \sqrt{1 - \rho^2} \left( p - p_0 - C_\Theta(\Theta - \Theta_0) \right), \qquad (59)$$

where $l_0$ is the half-length of the crack and $0 < \rho < 1$, for $\rho = x/l_0$ with $x$ being the distance to the origin of the crack. In three dimensions, the formula reads:

$$w(x,t) = \frac{4(1 - \nu_s^2)l_0}{\pi E} \sqrt{1 - \rho^2} \left( p - p_0 - C_\Theta(\Theta - \Theta_0) \right). \qquad (60)$$

For pressurized fracture without any thermal effect, i.e., $\Theta = \Theta_0 = 0$, we obtain the formulas derived in Sneddon and Lowengrub [44][Section 2.4 and Section 3.3].

- Fracture length and path for propagating fractures.

- Both stopping criteria of the nonlinear solver (Section 4.3), i.e. the relative residual norm and the active set constraint.

- For some fixed time steps, the average number of GMRES iterations within per Newton cycle.

- The evolution of the mechanical strain energy functional, i.e. mechanical term in Formulation 3.1 and dissipated fracture energy functional, i.e. the fracture term in Formulation 3.1.

- Comparisons regarding no split and vol./dev. split of strain density function.

21

### 5.4. Case a. Sneddon-Lowengrub's 2D setting with pressure

In the first example, we consider a stationary setting with a pressurized fracture. The geometrical setup is the same as illustrated in Fig. 3 and the material parameters are listed in Section 5.1.3. Related results were presented in [35, 47, 7].

We set the time step size $\delta t = 1\ s$ for a given constant pressure $\bar{p} = 10^{-3}\ KPa$. This test case is computed in a quasi-stationary manner: that is, we solve several pseudo-time steps. The goals of this test are to observe the crack opening displacement, and in particular to show the crack tip approximation. The initial mesh is five times uniformly refined, then, local mesh adaptivity is applied for five further levels.

The COD findings for both our computational model and the analytical calculation are shown in Fig. 6. It is observed the crack tips at $90m$ and $110m$ show excellent agreement with the analytical solution and convergence towards Sneddon-Lowengrubs manufactured solution.
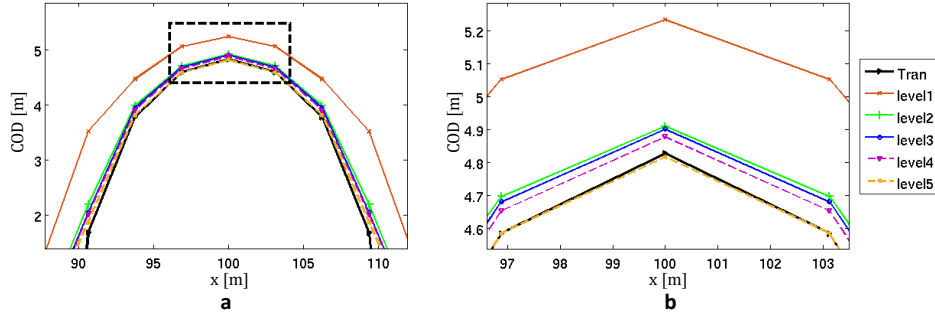


Figure 6: Case a. (a) COD for different global refinement level. (b) Zoom into the framed region on the left figure. Here the Tran et al. solution corresponds to the Sneddon-Lowengrub formula since no temperature is considered in this first example.

### 5.5. Case b. 2D setting with pressure and constant temperature

In this second example, we turn our attention now to a pressurized, non-isothermal configuration. Specifically, we follow Tran's et al. [45] 2D problem with a constant pressure and a fixed Hagoort's decline constant. We keep the geometry, all parameters, and tolerances as in the first example. Additionally, we set $\lambda_\Theta = 10^{-4}$ constant and we work still in a full stationary setting where the time step loop terminates after one step. The crack opening displacement both obtained through phase-field fracturing modeling and the analytical calculation are shown in Fig. 7 for the same refinement levels as in the previous example.
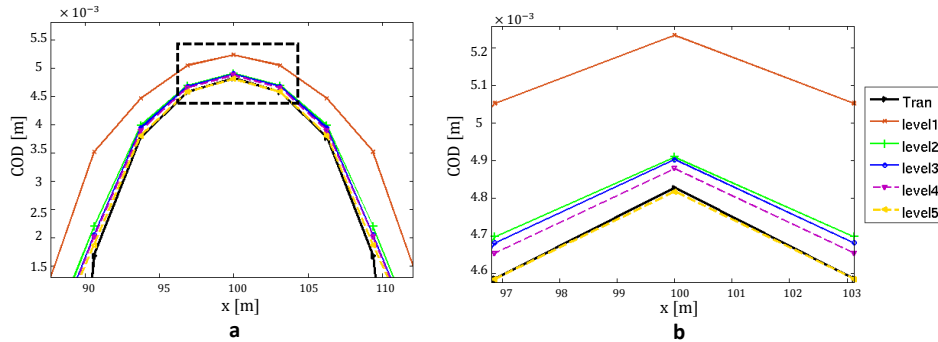


Figure 7: Case b. (a) COD for different refinement levels. (b) Zoom into the framed region on the left figure.

The crack phase-field pattern for different time steps on the locally adaptive refined meshes are illustrated in Fig. 8.
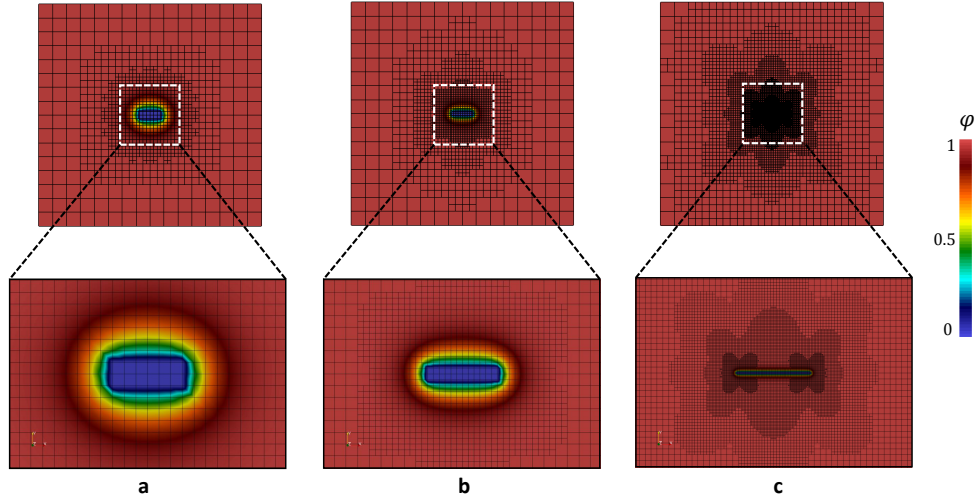
Figure 8: Case b. Crack phase-field resolution in the range of different time steps at time (a) 9 sec. (b) 14 sec. (c) 25 sec. on different locally refined meshes. Here, the fracture only varies in its width (i.e., COD), but not in length. Nonetheless, we perform time step solutions in order to fulfill the crack irreversibility constraint.

### 5.6. Case c. 2D setting with pressure, temperature and decline constant

While Hagoort's decline constants were constant in Case b, we now account for a temperature variation in time. We keep the geometry, all parameters, and tolerances as in the first example. The only two changes are that we set the time step size to one day $\delta t = 86400s$ and observe $T = 365$ days. This test case has a slight time-dependence since we use $\lambda_\Theta := \lambda_\Theta(t)$ being time-dependent and defined through Eq. 8. This scenario allows us to study the fracture behavior for a constant pressure like in the production processes.

Our numerical findings regarding the maximum COD is shown in Fig. 9. We consider different levels for uniformly refined meshes. Findings for level 5 and level 9 are shown in Fig. 9 a and b, respectively. In between we computed the levels 6-8 as well, but are not shown to keep the figures legibly. We observe excellent agreement of our numerical model with the analytical solution.
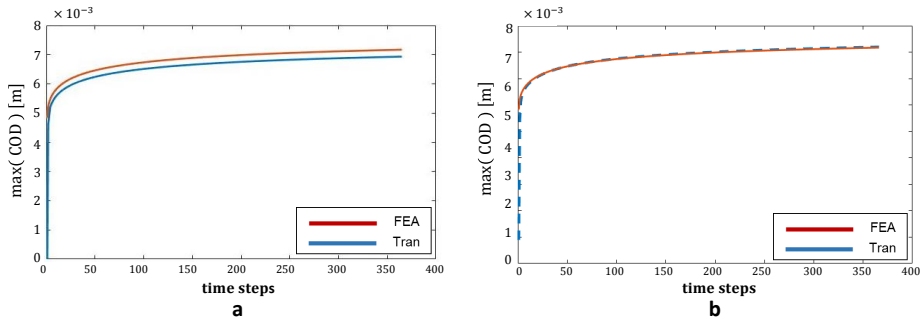


Figure 9: Case c. Maximum width evolution over time in the non-isothermal case. Injection of cold water $\Theta < \Theta_0$ leads to an increasing aperture over large time scales. (a) level 5 and (b) level 9 global refinement scheme.
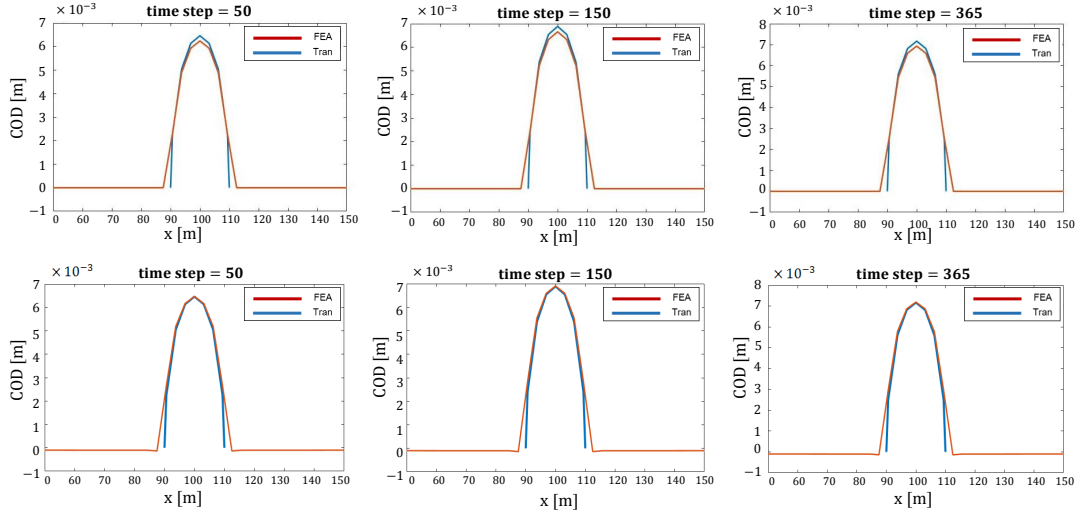
Figure 10: Case c. Comparison of the COD between phase-field numerical method and Tran's et al. [45] analytical solution during different time steps (a) first row corresponds to the level 5 and (b) second row corresponds to the level 9 global refinement scheme.

Another perception is to observe again the COD over the fracture (similar to Case a and Case b). This can be shown by fixing the time steps (i.e. 50, 150 and 365 days). Our findings are illustrated in Fig. 10 and show again excellent agreement.

### 5.7. Case d. 2D setting for the crack growth due to temperature variation

Having studied slight time dependencies with variations in the COD, we now consider a first test case with a propagating fracture. The propagation will be caused by temperature variations. For temperature variations, we use $\lambda_\Theta := \lambda_\Theta(t)$. Hagoort's decline constants for this example are shown in Fig. 11 a. The second novelty in this numerical test are comparisons of strain-energy split and the non-split version. The third goal are very detailed studies on the performance of the linear and nonlinear solvers.

Again, we keep most parameters as in the first example except a higher temperature difference to 220 degree Celsius (i.e. $\Theta_0 = 300\,C$ and $\Theta = 80\,C$) and the initial stress $p_0 = 12130$ KPa and constant pressure as mentioned earlier is set to $\bar{p} = 15834$ KPa.

In order to facilitate fracture propagation, the critical energy release rate is drastically reduced to $G_c = 5.5 \times 10^5\,N/m$. The time step size is $\delta t = 86400s$. As it is shown in Fig. 11 a, we are now interested in four specific time steps, namely 100, 114, 121 and 136 days.

### 5.7.1. Crack propagation and locally refined meshes

Figure 12 displays a sequence of crack patterns during different time steps without considering any strain-energy split, i.e. Formulation 2.3 and considering vol./dev. split, i.e. Formulation 3.1, of the strain energy density function. In fact, until time step 100, we observe almost no growth. Then, we have crack propagation towards the boundaries.
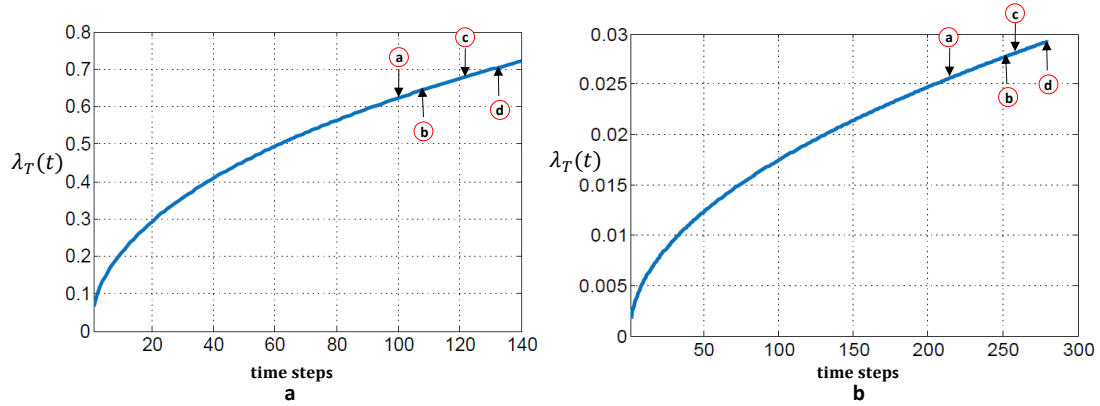
Figure 11: Hagoort's decline constants for a time-dependent problem that is $\lambda_\Theta := \lambda_\Theta(t)$, i.e. Eq. 8, for (a) Case d and (b) Case e. Interested time step steps for each cases are shown in each plot.
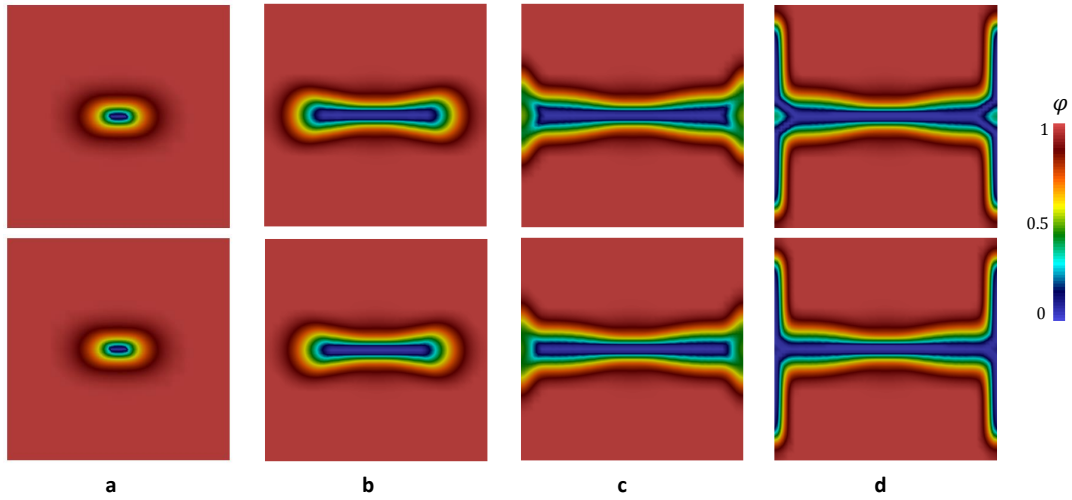


Figure 12: Case d. Crack phase-field evolution due to temperature variations at (a) 100 day (i.e $\lambda_\Theta = 0.6225$, $C_\Theta = 48933$) (b) 114 day ($\lambda_\Theta = 0.6596$, $C_\Theta = 50189$) (c) 121 day ($\lambda_\Theta = 0.6770$, $C_\Theta = 50751$) (d)136 day (i.e $\lambda_\Theta = 0.7121$, $C_\Theta = 51837$). First and second row represented for the no split and vol./dev. split of the strain energy density function, respectively.

The functionality of predictor-corrector mesh refinement is shown in Fig. 13 to present the evolution of the locally refined mesh when the crack is growing. As mentioned earlier in Section 5.1.4, $\text{Tol}_\varphi$ is set to 0.9. Each cell that has at least one support point with value $\varphi(x_i) < \text{Tol}_\varphi$ for $x_i \in \Omega_e$ will be refined unless we are already at the maximum desired refinement level is reached.

### 5.7.2. Analysis of the strain-energy splitting

We now turn to the second goal that is novel in this form in the published literature regarding pressurized/non-isothermal fracture settings with phase-field modeling.

A qualitative representation of the tensile and compression counterparts are shown in Fig. 14. We define $\theta_u := H^+(\nabla \cdot u) = H^+(tr(\varepsilon))$ that is an indicator to detect the compression region, i.e. $\theta_u < 0$, and, reversily, to detect the tensile region, i.e. $\theta_u > 0$. If the vol./dev. split of the strain energy density function is used, we are in the crack region when the phase-field energy exceeds its critical value $G_c$ and additionally $\theta_u > 0$. This gives us an additional constraint to our physical model. Hence, only the tensile stress is degraded and
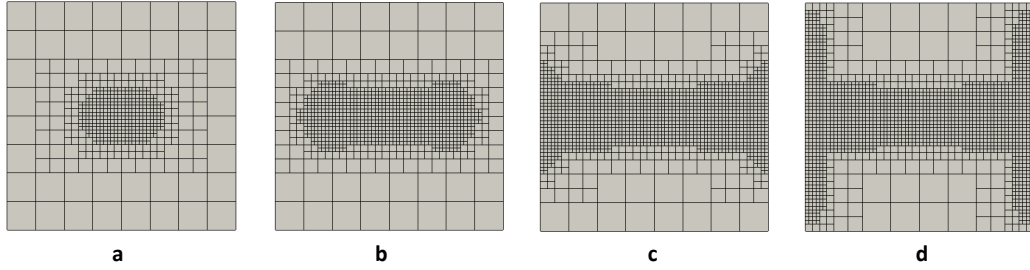
Figure 13: Case d. Functionality of predictor-corrector mesh refinement, i.e. the mesh evolves with the fracture. The transition zone with $0 < \varphi < 1$ determines the region in which the mesh has to be refined. $\texttt{Tol}_\varphi$ is set to 0.9. The refine meshes represent times steps (a) 100 day (b) 114 day (c) 121 day (d)136 day.

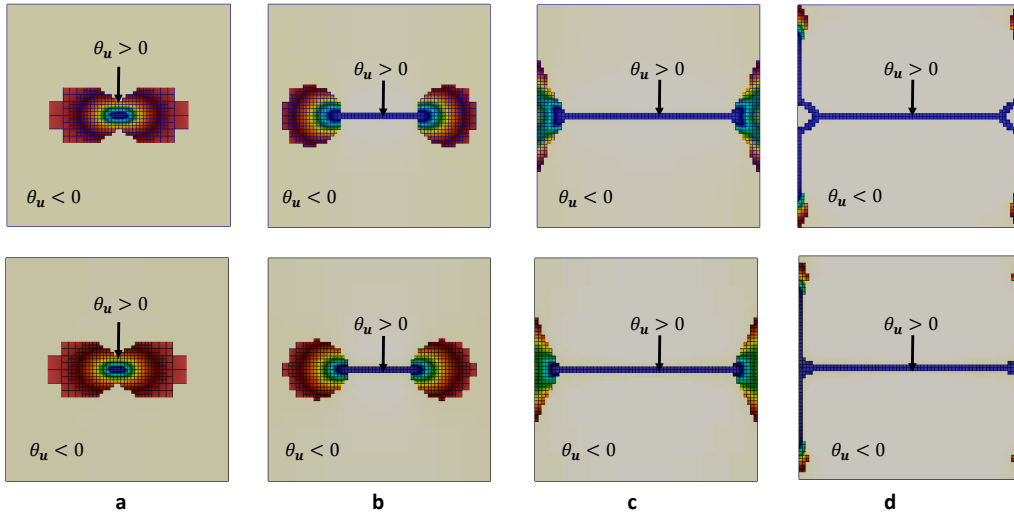compression stress is free from the effect of the phase-field variable; see Eq. 19.



Figure 14: Case d. Qualitative representation of the tensile and compression counterpart of domain. The compression region, i.e. $\theta_u := H^+(\nabla.u) < 0$, is shown uniformly in gray, and the tensile region, i.e. $\theta_u > 0$, is shown with desaturated rainbow colors at (a) 100 day (b) 114 day (c) 121 day (d) 136 day. The first row represents no splitting and the second row shows split of the strain energy density function.

Figure 15 compares the incremental elastic strain energy, i.e. the mechanical term in the Formulation 3.1, and the crack dissipated energy, i.e. fracture term in Formulation 3.1. For comparison, the strain energy density function without split and vol./dev. split are shown. As observed in Fig. 15, it turns out that dissipated fracture energy resulting from the crack phase-field evolution evolve with a sharp ascending behavior. This clearly shows that the sharp transition between the intact state and the fully cracked state of the solid body arised. Thereafter, dissipated fracture energy evolves towards a steady-state response. While the solid body completely fractured, no change in the dissipated fracture energy is observed anymore.

### 5.7.3. Performance of nonlinear and linear solvers

A detail analysis of the convergence of the primal-dual active set framework and the Newton solver are shown in Fig. 16 for the finest mesh level.

Finally, the average number of GMRES iterations of linear iterations per Newton cycle for different times steps is shown in Table 2. Specifically, the preconditioner (Section 4.5.2) works extremely well.
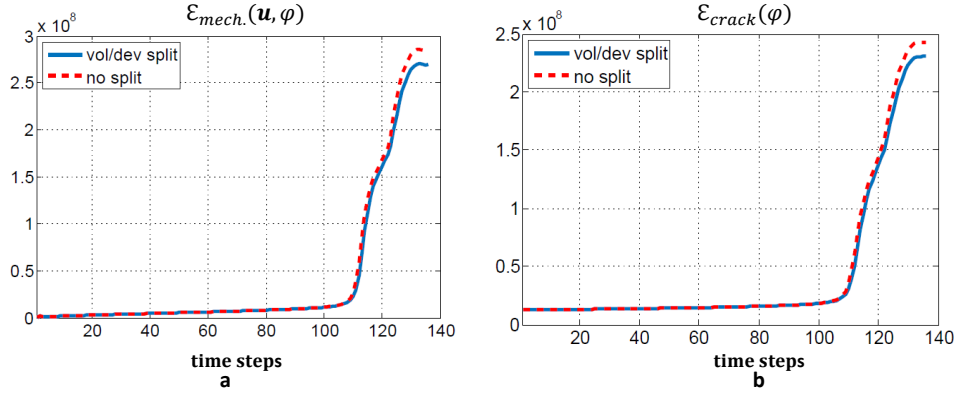
26

Figure 15: Case d. Plots over time of (a) the elastic strain energy per unit thickness, i.e. mechanical term in formulation 3.1 (b) the dissipated fracture energy per unit thickness , i.e. fracture term in formulation 3.1, with no split and vol./dev. split for strain energy density function.
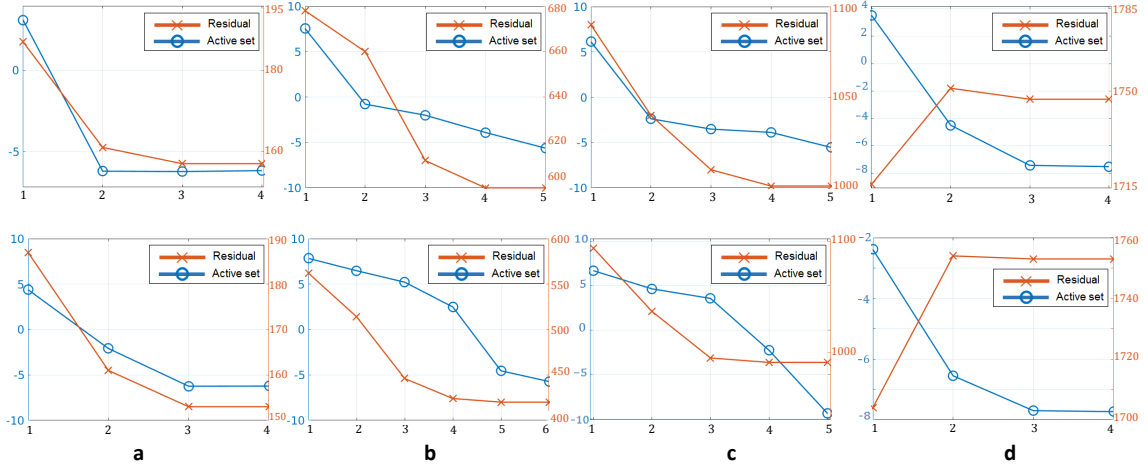


Figure 16: Case d. Performance of the combined Newton solver. Convergence behavior for the nonlinear relative residual, i.e. red line, and elements in the active set, i.e. blue line, at the fixed time steps (a) 100 day (b) 114 day (c) 121 day (d)136 day. The first row represents no splitting and the second row shows split of the strain energy density function.

Table 2: Case d. Average number of GMRES iterations for one Newton cycle for four different times steps.

| Time step (day) | no split | vol./ dev. split |
|---|---|---|
| 100 | 2 | 2 |
| 114 | 6 | 15 |
| 121 | 6 | 16 |
| 136 | 16 | 17 |

### 5.8. Case e. 2D setting for pressurized crack propagation in non-isothermal settings

In this example, we extend the previous Case d to study now crack propagation due to temperature effects , i.e. $\lambda_\Theta := \lambda_\Theta(t)$ and increasing pressure, i.e. $p := p(t)$. From the application viewpoint this example is closer to a fracture process with a characteristic time scale much smaller than in Case d. Hence, we set the

time step size to one day $\delta t = 60 s$ and simulate 270 minutes. The increasing pressure is prescribed as:

$$p := p(t) = \alpha(t + 1) \times \bar{p} = \alpha(t + 1)1.5834 \times 10^7, \quad \text{for} \quad t \geq 0. \tag{61}$$

We set the constant value $\alpha := \frac{1}{2}$ and $t$ is the time and given by $t = n\delta t$ with $n$ being the time step number. We keep all remaining parameters as in the first example and we set $\Theta_0 = 100 \, C$ and $\Theta = 70 \, C$ degree Celsius (recall $\Theta < \Theta_0$, see Remark 3.3).

### 5.8.1. Crack propagation and locally refined meshes

As shown in Fig. 17 b, we are now interested in four time steps, namely 240, 252, 259 and 267 minutes to observe the crack path. There again (as in Case d) only slight differences at the same points, suggesting that strain-splitting has nearly no effect in these configurations.
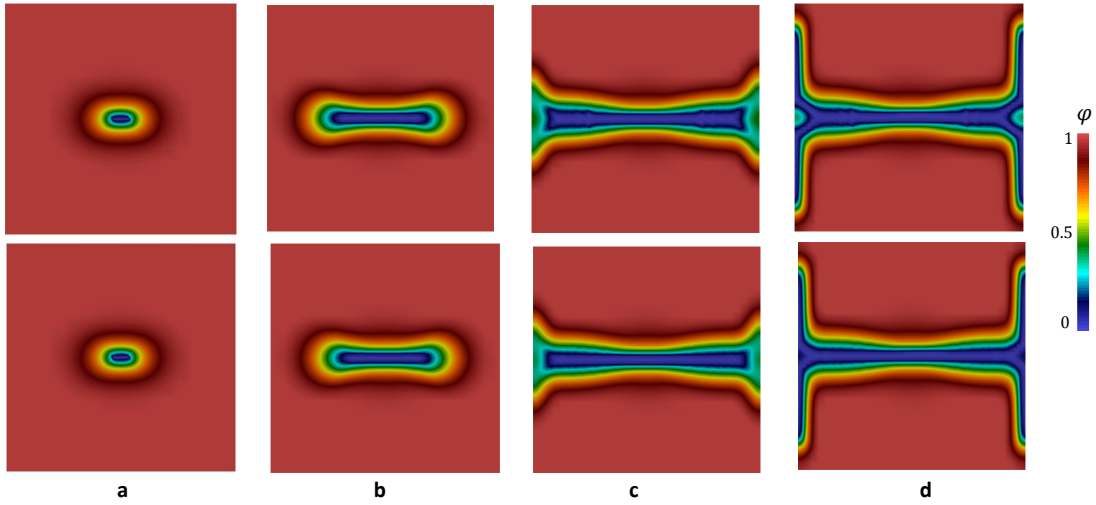


Figure 17: Case e. Crack phase-field evolution due to temperature and pressure variations at (a) 240 min (i.e. $\lambda_\Theta = 0.0271, C_\Theta = 4534, p = 1.9080 \times 10^9$) (b) 252 min (i.e. $\lambda_\Theta = 0.0278, C_\Theta = 4640.1, p = 2.0030 \times 10^9$) (c) 259 min (i.e. $\lambda_\Theta = 0.0281, C_\Theta = 4700.7, p = 2.0584 \times 10^9$) (d) 267 min (i.e. $\lambda_\Theta = 0.0286, C_\Theta = 4768.8, p = 2.1218 \times 10^9$). The first row represents no splitting and the second row shows split of the strain energy density function.

### 5.8.2. Analysis of the strain-energy splitting

A qualitative representation of the tensile region, i.e. $\theta_u > 0$, and compression counterpart, i.e. $\theta_u < 0$, are displayed in Fig. 18.

Based on the results, shown in Fig. 18 (and also Fig. 14), an alternative scalar variable for adaptive mesh refinement could be $\theta_u := H^+(\nabla.u)$ rather than using the phase-field variable. If $\theta_u = 1$, the material tends to tensile stress and hence crack propagation might occur and if $\theta_u = 0$ the material is under compression stress and we are away from the fracture zone. The main advantages of using $\theta_u$ rather than $\varphi \leq \text{TOL}_\varphi$ are two-fold. First, the above suggestion is based on the (physical) displacement field (and not on phase-field) and secondly, there is no requirement about choosing the correct threshold value for $\text{TOL}_\varphi$.

### 5.8.3. Performance of nonlinear and linear solvers

As in Case d, we study the solver performances. The evolution of the primal-dual active set and the Newton residuals are shown in Fig. 19.

The average number of GMRES iterations of linear iterations per Newton cycle for different times steps is shown in Table 3. Specifically, the preconditioner (Section 4.5.2) works again extremely well.
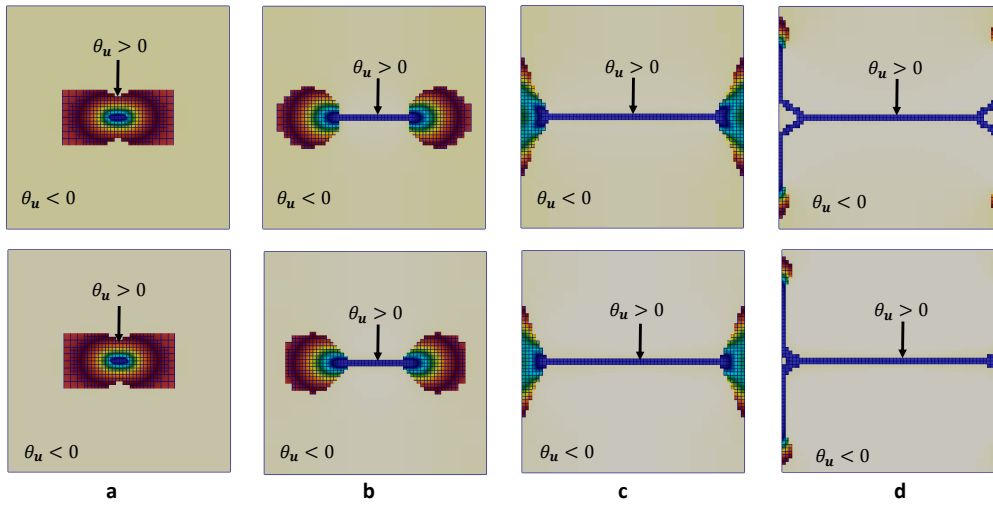
28

Figure 18: Case e. Qualitative representation of the tensile and compression counterpart of the domain at (a) 240 min (b) 252 min (c) 259 min (d)267 min.The first row represents no splitting and the second row shows split of the strain energy density function.
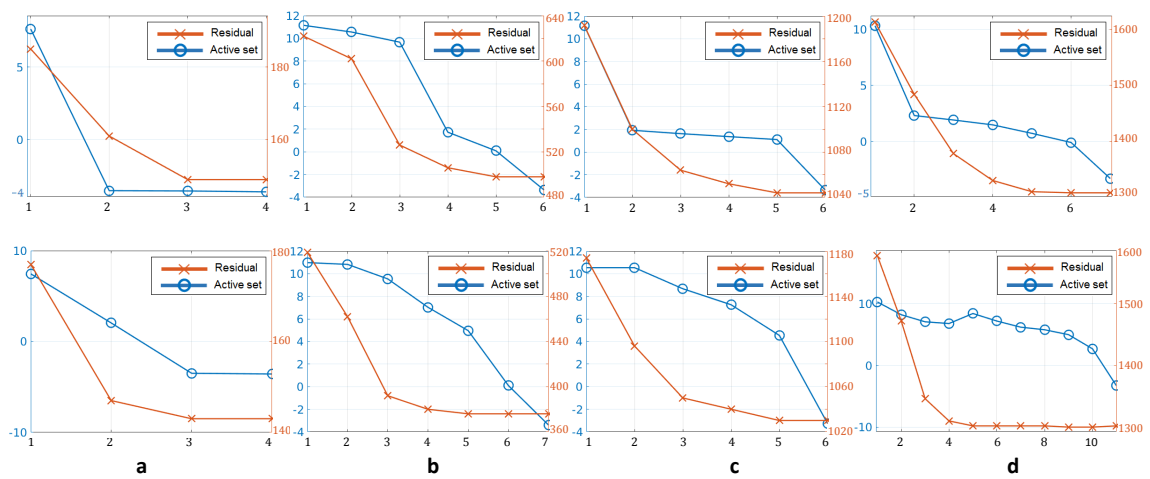


Figure 19: Case e. Performance of the combined Newton solver. Convergence behavior for the nonlinear relative residual, i.e. red line, and elements in the active set, i.e. blue line, at fixed time steps (a) 240 min (b) 252 min (c) 259 min (d) 267 min. The first row represents no splitting and the second row shows split of the strain energy density function.

Table 3: Case e. Average number of GMRES iterations per Newton cycle for different times steps.

| Time step (min) | no split | vol./dev. split |
|---|---|---|
| 240 | 2 | 2 |
| 252 | 10 | 14 |
| 259 | 4 | 17 |
| 267 | 13 | 24 |

29

## 5.9. Case f. 3D setting with pressure, temperature and decline constant

In this test, we extend Case c to a three-dimensional setting. The geometry and the material parameters are described in the Sections 5.1 and 5.6, respectively. The maximum width evolution is displayed in Figure 20 and shows a good fit with Tran's et al. [45] manufactured 3D solution for computing the maximal COD.
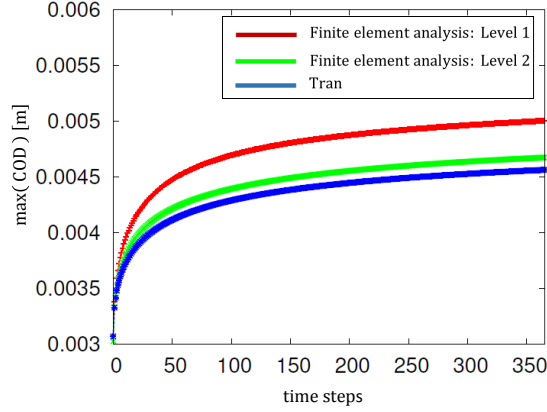


Figure 20: Case f. Maximum width evolution over time in the non-isothermal case. Injection of cold water $\Theta < \Theta_0$ leads to an increasing aperture over large time scales; here 365 days.

## 5.10. Case g. 3D setting for the Pressurized crack propagation in isothermal and non-isothermal settings

In this final example, the 2D Case e is extended to three dimensions. The geometry and material parameters are listed in the Sections 5.1 and 5.8. As in the 2D test case, the time step size is $\delta t = 60s$. We compute 27 loading (time) steps. The fracture radii are displayed in Figure 21. Graphical illustrations of the phase-field variable, i.e., the crack path, are displayed in Figure 22.
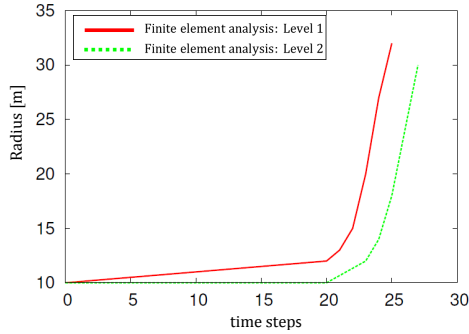


Figure 21: Case g. Radius evolution versus time on two spatial mesh refinement levels. We observe that the crack on the finer mesh starts a bit later to grow but on both refinement levels the growth velocity (i.e., the slope) is the same.
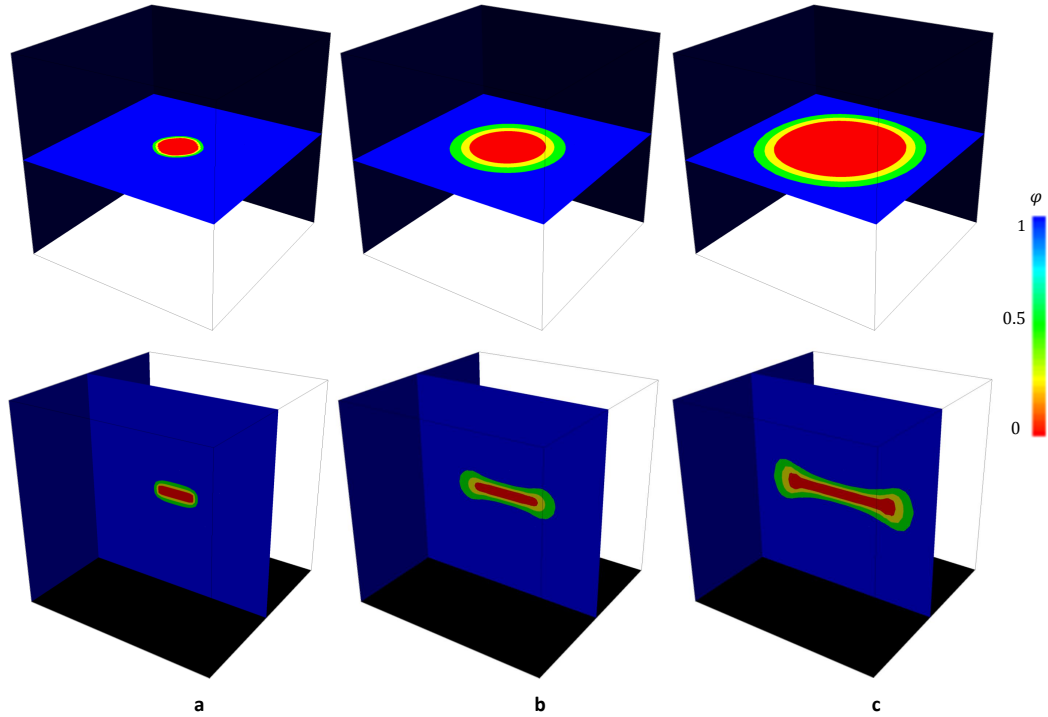
30

Figure 22: Case g. Penny-shaped crack phase-field evolution at three times (a) $t = 0$ min, (b) $t = 25$ min and (c) $t = 27$ min.

## 6. Conclusions

In this work, we developed a phase-field fracture model for pressurized and non-isothermal cracks in thermo-poroelasticity. We concentrated on the so-called mechanics step in which pressure and temperature are given quantities. Using the thermo-poroelastic stress tensor and interface laws, we derived an energy functional and the corresponding Euler-Lagrange equations. We then proceeded with a careful analysis from the mechanical point of view. As computational framework, we used a programming code that allows for adaptive mesh refinement and is fully parallelized. Therein, the nonlinear problem is formulated within a monolithic framework and is solved with a semi-smooth Newton method accounting as well for the crack irreversibility constraint. Based on these computational capacities, we ran in total seven test scenarios. Therein, we compared to analytical (manufactured) solutions taken from the literature with an excellent agreement of our numerical solutions. Moreover, we carried out mesh refinement studies and gave further insight into the performances of the linear and nonlinear solvers. In these studies, we also analyzed the effects on crack growth and solver behavior when strain-energy splitting is used or not. The outcome of our numerical simulations let us come to the conclusion that we have developed a robust and efficient computational framework for pressurized and non-isothermal configurations when the pressure and temperatures are given. In future studies, one idea is to treat the temperature as unknown to be determined by the governing partial differential equation. Here, we could proceed analogously to fluid-filled phase-field fracture models proposed in [36]. Another task will be more computations of practical problems with multiple interacting fractures.

# References

[1] M. Ambati, T. Gerasimov, and L. D. Lorenzis. A review on phase-field models of brittle fracture and a new fast hybrid formulation. *Computational Mechanics*, 55(2):383–405, 2015.

[2] L. Ambrosio and V. Tortorelli. Approximation of functionals depending on jumps by elliptic functionals via $\gamma$-convergence. *Comm. Pure Appl. Math.*, 43:999–1036, 1990.

[3] L. Ambrosio and V. Tortorelli. On the approximation of free discontinuity problems. *Boll. Un. Mat. Ital. B*, 6:105–123, 1992.

[4] H. Amor, J.-J. Marigo, and C. Maurini. Regularized formulation of the variational brittle fracture with unilateral contact: Numerical experiments. *J. Mech. Phys. Solids*, 57:1209–1229, 2009.

[5] D. Arndt, W. Bangerth, D. Davydov, T. Heister, L. Heltai, M. Kronbichler, M. Maier, J.-P. Pelteret, B. Turcksin, and D. Wells. The `deal.II` library, version 8.5. *Journal of Numerical Mathematics*, 2017.

[6] W. Bangerth, R. Hartmann, and G. Kanschat. deal.II – a general purpose object oriented finite element library. *ACM Trans. Math. Softw.*, 33(4):24/1–24/27, 2007.

[7] B. Bourdin, C. Chukwudozie, and K. Yoshioka. A variational approach to the numerical simulation of hydraulic fracturing. SPE Journal, Conference Paper 159154-MS, 2012.

[8] B. Bourdin, G. Francfort, and J.-J. Marigo. Numerical experiments in revisited brittle fracture. *J. Mech. Phys. Solids*, 48(4):797–826, 2000.

[9] B. Bourdin, G. Francfort, and J.-J. Marigo. The variational approach to fracture. *J. Elasticity*, 91(1–3):1–148, 2008.

[10] B. Bourdin, G. A. Francfort, and J. J. Marigo. Numerical experiments in revisited brittle fracture. *Journal of the Mechanics and Physics of Solids*, 48:797–826, 2000.

[11] B. Bourdin, J.-J. Marigo, C. Maurini, and P. Sicsic. Morphogenesis and propagation of complex cracks induced by thermal shocks. *Phys. Rev. Lett.*, 112:014301, Jan 2014.

[12] R. M. Charlotte Kuhn, Alexander Schlter. On degradation functions in phase field fracture models. *Computational Materials Science*, 108:374–384, 2015.

[13] K. Chun. Fracture propagation under poro-thermally induced stress using the displacement discontinuity method. Technical Report Proceedings, Thirty-Eight Workshop in Geothermal Reservoir Engineering, Stanford University, 2013.

[14] P. G. Ciarlet. *The finite element method for elliptic problems*. North-Holland, Amsterdam [u.a.], 2. pr. edition, 1987.

[15] O. Coussy. *Poromechanics*. Wiley, 2004.

[16] N. G. Doonechaly, R. A. Azim, and S. Rahman. A study of permeability changes due to cold fluid circulation in fractured geothermal reservoirs. *Ground Water.*, 54(3):325–35, 2016.

[17] P. Farrell and C. Maurini. Linear and nonlinear solvers for variational phase-field models of brittle fracture. *International journal for numerical method in engineering*, 109:648–667, 2017.

[18] G. Francfort and J.-J. Marigo. Revisiting brittle fracture as an energy minimization problem. *J. Mech. Phys. Solids*, 46(8):1319–1342, 1998.

[19] T. Gerasimov and L. D. Lorenzis. A line search assisted monolithic approach for phase-field computing of brittle fracture. *Computer Methods in Applied Mechanics and Engineering*, 312:276 – 303, 2016.

[20] T. Gerasimov, N. Noii, O. Allix, and L. D. Lorenzis. A non-intrusive global/local approach applied to phase-field modeling of brittle fracture. *Advanced Modeling and Simulation in Engineering Sciences*, 14, 2018.

[21] A. Ghassemi and G. Kumar. Changes in fracture aperture and fluid pressure due to thermal stress and silica dissolution/precipitation induced by heat extraction from subsurface rocks. *Geothermics*, 36:115–140, 2006.

[22] A. Ghassemi and Q. Zhang. Porothermoelastic analysis of the response of a stationary crack using the displacment discontinuity method. *Journal of Engineering Mechanics*, 132:26–33, 2006.

[23] J. Hagoort. Waterflood-induced hydraulic fracturing. Technical Report PhD Dissertation, Delft, The Netherlands, 1981.

[24] T. Heister, M. F. Wheeler, and T. Wick. A primal-dual active set method and predictor-corrector mesh adaptivity for computing fracture propagation using a phase-field approach. *Comp. Meth. Appl. Mech. Engrg.*, 290(0):466 – 495, 2015.

[25] T. Heister and T. Wick. Parallel solution, adaptivity, computational convergence, and open-source code of 2d and 3d pressurized phase-field fracture problems. https://arxiv.org/abs/1806.09924, accepted in PAMM, 2018.

[26] M. A. Heroux, R. A. Bartlett, V. E. Howle, R. J. Hoekstra, J. J. Hu, T. G. Kolda, R. B. Lehoucq, K. R. Long, R. P. Pawlowski, E. T. Phipps, A. G. Salinger, H. K. Thornquist, R. S. Tuminaro, J. M. Willenbring, A. Williams, and K. S. Stanley. An overview of the trilinos project. *ACM Trans. Math. Softw.*, 31(3):397–423, 2005.

[27] N. Kikuchi and J. Oden. *Contact problems in elasticity*. Studies in Applied Mathematics. Society for Industrial and Applied Mathematics (SIAM), Philadelphia, PA, 1988.

[28] D. Kinderlehrer and G. Stampacchia. *An Introduction to Variational Inequalities and Their Applications*. Classics in Applied Mathematics. Society for Industrial and Applied Mathematics, 2000.

[29] S. Lee, M. F. Wheeler, and T. Wick. Pressure and fluid-driven fracture propagation in porous media using an adaptive finite element phase field model. *Computer Methods in Applied Mechanics and Engineering*, 305:111 – 132, 2016.

[30] C. Miehe, M. Hofacker, L.-M. Schaenzel, and F. Aldakheel. Phase field modeling of fracture in multi-physics problems. part ii. coupled brittle-to-ductile failure criteria and crack propagation in thermo-elasticplastic solids. *Computer Methods in Applied Mechanics and Engineering*, 294:486 – 522, 2015.

[31] C. Miehe, M. Hofacker, and F. Welschinger. A phase field model for rate-independent crack propagation: Robust algorithmic implementation based on operator splits. *Comput. Meth. Appl. Mech. Engrg.*, 199:2765–2778, 2010.

[32] C. Miehe, L.-M. Schaenzel, and H. Ulmer. Phase field modeling of fracture in multi-physics problems. part i. balance of crack surface and failure criteria for brittle crack propagation in thermo-elastic solids. *Computer Methods in Applied Mechanics and Engineering*, 294:449 – 485, 2015.

[33] C. Miehe, F. Welschinger, and M. Hofacker. Thermodynamically consistent phase-field models of fracture: variational principles and multi-field fe implementations. *International Journal of Numerical Methods in Engineering*, 83:1273–1311, 2010.

[34] A. Mikelić, M. Wheeler, and T. Wick. A phase-field approach to the fluid filled fracture surrounded by a poroelastic medium. ICES Report 13-15, Jun 2013.

[35] A. Mikelić, M. Wheeler, and T. Wick. Phase-field modeling through iterative splitting of hydraulic fractures in a poroelastic medium. Accepted for publication in GEM - International Journal on Geomathematics, Oct 2018.

[36] A. Mikelić, M. F. Wheeler, and T. Wick. A phase-field method for propagating fluid-filled fractures coupled to a surrounding porous medium. *SIAM Multiscale Model. Simul.*, 13(1):367–398, 2015.

[37] K. Pham, H. Amor, J.-J. Marigo, and C. Maurini. Gadient damage models and their use to approximate brittle fracture. *Int. J. Damage Mech*, 4:618–652, 2011.

[38] K. Pruess and J. S. Y. Wang. *Numerical Modeling of Isothermal and Nonisothermal Flow in Unsaturated Fractured Rock: A Review*, pages 19–32. American Geophysical Union (AGU), 2013.

[39] J. Rice. Mathematical analysis in the mechanics of fracture. 1968.

[40] S. Salimzadeh, A. Paluszny, H. M. Nick, and R. W. Zimmerman. A three-dimensional coupled thermo-hydro-mechanical model for deformable fractured geothermal systems. *Geothermics*, 71:212 – 224, 2018.

[41] S. Salimzadeh, A. Paluszny, and R. W. Zimmerman. Effect of cold co2 injection on fracture apertures and growth. *International Journal of Greenhouse Gas Control*, 74:130 – 141, 2018.

[42] S. Shiozawa, S. Lee, and M. Wheeler. The effect of stress boundary conditions on fluid-driven fracture propagation in porous media using a phase field modeling approach. in revision, 2019.

[43] I. N. Sneddon. The distribution of stress in the neighbourhood of a crack in an elastic solid. *Proc. R Soc London A*, 187:229–260, 1946.

[44] I. N. Sneddon and M. Lowengrub. *Crack problems in the classical theory of elasticity*. SIAM series in Applied Mathematics. John Wiley and Sons, Philadelphia, 1969.

[45] D. Tran, A. T. Settari, and L. Nghiem. Predicting growth and decay of hydraulic-fracture witdh in porous media subjected to isothermal and nonisothermal flow. *SPE-J*, pages 781–794, 2013.

[46] Y. Wang and E. Papamichos. Thermal effects on fluid flow and hydraulic fracturing from wellbores and cavities in low-permeability formations. *Int. J. Numer. Analytical Methods Geomechanics*, 23:1819–1834, 1999.

[47] M. Wheeler, T. Wick, and W. Wollner. An augmented-Lagangrian method for the phase-field approach for pressurized fractures. *Comp. Meth. Appl. Mech. Engrg.*, 271:69–85, 2014.

[48] T. Wick. An error-oriented Newton/inexact augmented Lagrangian approach for fully monolithic phase-field fracture propagation. *SIAM Journal on Scientific Computing*, 39(4):B589–B617, 2017.

[49] T. Wick. Modified Newton methods for solving fully monolithic phase-field quasi-static brittle fracture propagation. *Computer Methods in Applied Mechanics and Engineering*, 325:577 – 611, 2017.

[50] T. Wick, S. Lee, and M. Wheeler. 3D phase-field for pressurized fracture propagation in heterogeneous media. ECCOMAS and IACM Coupled Problems Proc., May 2015 at San Servolo, Venice, Italy, 2015.